Monthly Notices of the ROYAL ASTRONOMICAL SOCIETY

MNRAS **438,** 1267–1287 (2014) doi:10.1093/mnras/stt2273
Advance Access publication 2013 December 17

An ALMA survey of sub-millimetre Galaxies in the Extended *Chandra* Deep Field South: the far-infrared properties of SMGs

A. M. Swinbank,[1⋆] J. M. Simpson,[1] Ian Smail,[1] C. M. Harrison,[1] J. A. Hodge,[2] A. Karim,[3] F. Walter,[2] D. M. Alexander,[1] W. N. Brandt,[4] C. de Breuck,[5] E. da Cunha,[2] S. C. Chapman,[6] K. E. K. Coppin,[7] A. L. R. Danielson,[1] H. Dannerbauer,[8] R. Decarli,[2] T. R. Greve,[9] R. J. Ivison,[10] K. K. Knudsen,[11] C. D. P. Lagos,[5] E. Schinnerer,[2] A. P. Thomson,[1] J. L. Wardlow,[12] A. Weiß[13] and P. van der Werf[14]

[1]*Institute for Computational Cosmology, Durham University, South Road, Durham DH1 3LE, UK*
[2]*Max-Planck-Institut für Astronomie, Königstuhl 17, D-69117 Heidelberg, Germany*
[3]*Argelander-Institute of Astronomy, Bonn University, Auf dem Huegel 71, D-53121 Bonn, Germany*
[4]*Department of Astronomy and Astrophysics, 525 Davey Lab, The Pennsylvania State University, University Park, PA 16802, USA*
[5]*European Southern Observatory, Karl-Schwarzschild Strasse 2, D-85748 Garching, Germany*
[6]*Dalhousie University, Halifax, Nova Scotia B3H 4R2, Canada*
[7]*Centre for Astrophysics Research, University of Hertfordshire, College Lane, Hatfield, Herts AL10 9AB, UK*
[8]*Universität Wien, Institut für Astrophysik, Türkenschanzstraße 17, A-1180 Wien, Austria*
[9]*University College London, Department of Physics and Astronomy, Gower Street, London WC1E 6BT, UK*
[10]*Institute for Astronomy, University of Edinburgh, Blackford Hill, Edinburgh EH9 3HJ, UK*
[11]*Department of Earth and Space Sciences, Chalmers University of Technology, Onsala Space Observatory, SE-43992 Onsala, Sweden*
[12]*Dark Cosmology Centre, Niels Bohr Institute, University of Copenhagen, Juliane Maries Vej 30, DK-2100 Copenhagen, Denmark*
[13]*Max-Planck-Institut für Radioastronomie, Auf dem Hügel 69, D-53121 Bonn, Germany*
[14]*Leiden Observatory, Leiden University, PO Box 9513, NL-2300 RA Leiden, the Netherlands*

Accepted 2013 November 21. Received 2013 November 21; in original form 2013 October 21

ABSTRACT

We exploit Atacama Large Millimeter Array (ALMA) 870 μm observations of sub-millimetre sources in the Extended *Chandra* Deep Field South to investigate the far-infrared properties of high-redshift sub-millimetre galaxies (SMGs). Using the precisely located 870 μm ALMA positions of 99 SMGs, together with 24μm and radio imaging, we deblend the *Herschel*/SPIRE imaging to extract their far-infrared fluxes and colours. The median redshifts for ALMA LESS (ALESS) SMGs which are detected in at least two SPIRE bands increases with wavelength of the peak in their spectral energy distributions (SEDs), with $z = 2.3 \pm 0.2$, 2.5 ± 0.3 and 3.5 ± 0.5 for the 250, 350 and 500 μm peakers, respectively. 34 ALESS SMGs do not have a $>3\sigma$ counterpart at 250, 350 or 500 μm. These galaxies have a median photometric redshift derived from the rest-frame UV–mid-infrared SEDs of $z = 3.3 \pm 0.5$, which is higher than the full ALESS SMG sample; $z = 2.5 \pm 0.2$. We estimate the far-infrared luminosities and characteristic dust temperature of each SMG, deriving $L_{\rm IR} = (3.0 \pm 0.3) \times 10^{12}\,{\rm L}_{\odot}$ (SFR $= 300 \pm 30\,{\rm M}_{\odot}\,{\rm yr}^{-1}$) and $T_{\rm d} = 32 \pm 1$ K. The characteristic dust temperature of these high-redshift SMGs is $\Delta T_{\rm d} = 3$–5 K lower than comparably luminous galaxies at $z = 0$, reflecting the more extended star formation in these systems. We show that the contribution of $S_{870\,\mu{\rm m}} \geq 1$ mJy SMGs to the cosmic star formation budget is 20 per cent of the total over the redshift range $z \sim 1$–4. Adopting an appropriate gas-to-dust ratio, we estimate a typical molecular mass of the ALESS SMGs of $M_{\rm H_2} = (4.2 \pm 0.4) \times 10^{10}\,{\rm M}_{\odot}$. Finally, we show that SMGs with $S_{870\,\mu{\rm m}} > 1$ mJy ($L_{\rm IR} \gtrsim 10^{12}\,{\rm L}_{\odot}$) contain ~ 10 per cent of the $z \sim 2$ volume-averaged H_2 mass density.

Key words: galaxies: evolution – galaxies: high-redshift – galaxies: starburst.

⋆ E-mail: a.m.swinbank@dur.ac.uk

1 INTRODUCTION

Ultraluminous Infrared Galaxies (ULIRGs; Sanders & Mirabel 1996) have total infrared (IR) luminosities $>10^{12-13}\,L_{\odot}$ and implied star formation rates (SFR) $>$ 100–1000 $M_{\odot}\,yr^{-1}$. Their low space densities mean that ULIRGs contribute $\ll$1 per cent of the volume average star formation density at $z = 0$. However, the first deep, single-dish bolometer surveys in the 870 μm atmospheric window uncovered high number densities of high-redshift sub-mm galaxies (SMGs) at mJy flux density levels (Smail, Ivison & Blain 1997; Barger et al. 1998; Hughes et al. 1998). Subsequent spectroscopic studies of the radio-/mid-IR detected sub-set of the population gave a median redshift of $z \sim 2.5$ (Chapman et al. 2005), confirming their ULIRG-like luminosities (Kovács et al. 2006; Coppin et al. 2008a; Magnelli et al. 2012a) and demonstrated that ULIRGs undergo a 1000-fold increase in space density from $z = 0$ to $z \sim 2.5$. Thus, in contrast to the local Universe, ULIRGs are a non-negligible component of the star-forming population at $z \sim 2$–3 (e.g. Hughes et al. 1998; Blain et al. 1999; Lilly et al. 1999; Chapman et al. 2005; Wardlow et al. 2011; Barger et al. 2012; Casey et al. 2013).

These 870 μm selected samples remain the best-studied SMGs, and links have been proposed between SMGs, quasi-stellar objects and the formation phase of massive galaxies at high redshift (e.g. Genzel et al. 2003; Swinbank et al. 2006; Coppin et al. 2008b; Daddi et al. 2009; Hickox et al. 2012). SMGs are therefore a potentially important element in models of galaxy formation. However, these evolutionary links are still unproven, although it is clear that most luminous SMGs lie above the purported 'main sequence' of star-forming galaxies in the SFR–$M_{\star}$ plane (e.g. Daddi et al. 2007; Noeske et al. 2007; Rodighiero et al. 2011; Wardlow et al. 2011). Along with corroborating kinematic and morphological evidence (Tacconi et al. 2006, 2008; Engel et al. 2010; Swinbank et al. 2010; Alaghband-Zadeh et al. 2012), inevitably it has been argued that SMGs can be understood as 'scaled-up' analogues of local ULIRGs which are dominated by merger-induced starbursts. It has also been proposed that lower luminosity SMGs overlap with the 'main sequence', leading to claims of an apparent dichotomy within this population, i.e. between a true 'starburst' population and slightly less active galaxies, potentially driven by secular processes (Rodighiero et al. 2011).

Theoretical attempts to reproduce basic properties of SMGs, such as 870 μm number counts, have also led to an equally wide variety of conclusions about the nature and diversity of this population. For example, early models from Baugh et al. (2005) and Granato et al. (2006) include two recipes for star formation; 'burst' and 'quiescent', with SMGs corresponding to the most extreme starburst systems. One key strength of these models is that they are also required to fit the galaxy population at $z = 0$, which forces the former to adopt a burst initial mass function (IMF) biased to high-mass stars (allowing relatively low-mass galaxies to produce intense starbursts; Baugh et al. 2005). In contrast, numerical models of Hayward et al. (2011; see also Narayanan et al. 2009 and Davé et al. 2010) suggest that SMGs are dominated by secular bursts in gas-rich disc galaxies, with 'standard' IMFs. Hence theoretical models variously predict the SMG population to comprise low-mass merging starbursts (with unusually low mass-to-light ratios; e.g. Baugh et al. 2005) and isolated, gas-rich disc galaxies undergoing secular bursts (e.g. Davé et al. 2010; Hayward et al. 2012).

This rich array of theoretical options demonstrates the power of SMGs to distinguish between the competing galaxy evolution theories. Observations of the most basic properties of SMGs, such as their redshift distribution, bolometric luminosities, cold molecular gas dynamics and gas mass, and contribution to the cosmic star formation density should have the power to distinguish between the theoretical models.

However, the coarse resolution of single dish sub-mm telescopes (typically ∼15–20 arcsec) means that identifying the SMG counterparts has to date, relied on correlations between their sub-millimetre emission and that in other wavebands where higher spatial resolution is available (usually the radio and/or mid-IR; e.g. Ivison et al. 2002, 2005, 2007; Pope et al. 2006). The spectral energy distributions (SEDs) in these other wavebands have positive *K*-corrections, making counterparts which either lie at higher redshift or that have colder-than-average dust temperatures impossible to identify. Indeed, in sub-millimetre surveys typically 40–50 per cent of sub-mm sources lack 'robust' counterparts in the radio or mid-IR (e.g. Biggs et al. 2011, see also Lindner et al. 2011) and it is unknown whether the unidentified SMGs have the same redshift distribution (or are representative) of the radio-identified sub-set, potentially biasing the current observational results.

To circumvent the problem of missing- (and mis-) identifications and so characterize the *whole* population of bright SMGs in an unbiased manner requires precisely locating the sub-mm emission using sub/mm interferometers (e.g. Wang et al. 2011; Smolčić et al. 2012). Recently, we have undertaken an Atacama Large Millimeter Array (ALMA) survey of the 126 sub-mm sources in the 0.°5 × 0.°5 Extended *Chandra* Deep Field South (ECDFS), taken from the 'LESS' survey (Weiß et al. 2009). The ALMA data precisely locate the SMGs, *directly* pin-pointing the source(s) responsible for the sub-mm emission (to within $<$0.3 arcsec), without recourse to statistical radio/mid-IR associations and so yielding unambiguous identifications for the majority of the SMGs. The first results from our survey include the source catalogue and multiplicity of bright SMGs (Hodge et al. 2013); the first high-resolution sub-mm counts (Karim et al. 2013); optical and near-IR properties, photometric redshift distribution and stellar masses (Simpson et al. 2013); serendipitous identification [C II] at $z = 4.4$ in two SMGs (Swinbank et al. 2012) and subsequent ^{12}CO follow-up in these galaxies (Huynh et al. 2013); X-ray properties and AGN fraction of ALMA SMGs (Wang et al. 2013); far-IR–radio correlation of SMGs (Thomson et al. 2014 submitted) and *Hubble Space Telescope* (*HST*) morphologies (Simpson et al., in preparation).

In this paper, we extend these analyses and exploit the *Herschel* Space Observatory PACS and SPIRE imaging of the ECDFS to derive the far-IR/sub-millimeter properties of the SMGs pinpointed by ALMA. In particular, we use the far-IR (70–870 μm) and 1.4 GHz radio photometry together with new optical/mid-IR-derived photometric redshifts from Simpson et al. (2013) to derive the far-IR luminosities, characteristic dust temperatures, dust masses and investigate their evolution with redshift. In Section 2, we describe the observations and deblending techniques; in Section 3, we present the far-IR properties (colours, luminosities, dust masses) of both individual ALESS SMGs and those of the stacks of sub-sets of population. We present our main conclusions in Section 4. Throughout the paper, we adopt a Chabrier IMF (Chabrier 2003) and use a Λ cold dark matter cosmology (Spergel et al. 2007) with $\Omega_{\Lambda} = 0.73$, $\Omega_{\rm m} = 0.27$ and $H_0 = 72\,{\rm km\,s^{-1}\,Mpc^{-1}}$.

2 OBSERVATIONS AND ANALYSIS

2.1 ALMA

Details of the ALMA observations of the sub-millimeter sources from the ALMA LESS (ALESS) survey are described in Hodge et al.

(2013; see also Karim et al. 2013). Briefly, observations of 122 of the 126 LESS sources were obtained with ALMA in Cycle 0 at 345 GHz (Band 7) with a dual polarization setup in the compact configuration (yielding a synthesized beam of $\sim$1.6 arcsec $\times$ 1.2 arcsec). The ALMA primary beam, 17.3 arcsec full width at half-maximum (FWHM) at our observing frequency, is sufficient to encompass the error-circles of the sub-millimeter sources from the LESS maps, $\lesssim$5 arcsec (Weiß et al. 2009). The observations employed 12–15 antennas and were obtained between 2011 October and 2011 November in good conditions, PWV $\lesssim$ 0.5 mm. Phase and bandpass calibration was based on J0403−360, J0538−440, respectively, and flux calibration performed on available planets at the time of observation. The data were processed with the Common Astronomy Software Application (CASA; McMullin et al. 2007). The resulting velocity integrated continuum maps reach typical noise levels of $\sigma = 0.4$–0.5 mJy beam^{-1}, a factor of $\sim$3$\times$ more sensitive than the original LABOCA discovery map and, critically, with a beam that is $\sim$200 $\times$ smaller in area than that of LABOCA.

From the ALMA maps, Hodge et al. (2013) extract 99 SMGs with S/N $>$ 3.5 from the best maps (noise $<$0.6 mJy and synthesized beam with axial ratio $<$2). This selection provides an acceptable trade-off between source reliability and spurious sources. Indeed, using the background fluctuations in the map, Karim et al. (2013) demonstrate that we expect only one SMG in the catalogue to be spurious and one SMG to be missed. We note that Hodge et al. (2013) also provide a catalogue of a further 32 ALMA SMGs which are from either the shallower maps (noise levels $\sigma < 0.6$–1.0 mJy), or $>4\sigma$ sources within 2$\times$ the primary beam of the best maps, but these 'supplementary' catalogues are expected to have lower completeness and a higher spurious fraction and so conservatively we do not use these sources in our analysis here.

2.2 1.4 GHz VLA Radio and 24 μm *Spitzer* Imaging

The ECDFS was observed with the Jansky Very Large Array in D, C, B and A configurations in 2007 June to September, reaching an rms of $\sigma_{1.4\,\mathrm{GHz}} = 8.3$ μJy with a synthesized beam of 2.8 arcsec $\times$ 1.6 arcsec. These data and catalogues are described in detail in Miller et al. (2013; see also Biggs et al. 2011).

Spitzer/MIPS 24 μm imaging is also available for the ECDFS as part of the Far-Infrared Deep Extragalactic Legacy (FIDEL) survey. This MIPS 24 μm imaging provides an important addition in the construction of a positional prior catalogue which is used to deblend the *Herschel* images (see Section 2.3.1) as well as providing a constraint used in the far-IR SEDs of the ALMA SMGs. We obtained the reduced MIPS 24 μm images of the ECDFS from the NASA Infrared Astronomy Archive[1]. This imaging covers the entire ECDFS survey area, and we extract a catalogue of $\sim$3600 sources in the ECDFS down to a 5σ depth of $\sim$56 μJy (aperture corrected).

2.3 Herschel/PACS and SPIRE Imaging

Herschel/PACS observations covering the ECDFS at 100 and 160 μm and the CDFS at 70, 100 and 160 μm were taken as part of the PACS Evolutionary Probe (PEP) survey (the CDFS lies in the central 0.11-square degrees of the ECDFS). These data and deblended catalogues are described in Lutz et al. (2011) and Magnelli et al. (2013) and reach 1σ sensitivities of 0.2–0.4 mJy (CDFS) and 1–2.6 mJy (ECDFS). We match our ALESS catalogue with those from Magnelli et al. (2013) (with a matching radius of 1.5 arcsec) and include the 70–160 μm photometry for the ALESS SMGs from the CDFS and the ECDFS wherever possible in our analysis below.

Herschel/SPIRE 250, 350 and 500 μm observations covering ECDFS were taken as part of the *Herschel* Multitiered Extragalactic Survey (HerMES) guaranteed time programme (as described in Oliver et al. 2012). In total, ECDFS was observed for 32.4 ks at 250, 350 and 500 μm in $\sim$1.8 ks blocks. For each observation, we retrieved the Level 2 data product from the *Herschel* European Space Agency (ESA) archive and aligned and co-added the maps. The final combined maps reach a 1σ noise level of 1.6, 1.3 and 1.9 mJy at 250, 350 and 500 μm, respectively (see Oliver et al. 2012, for a detailed description of the observations).

To align the SPIRE maps to the ALMA and radio astrometry, we aligned the SPIRE maps at 250, 350 and 500 μm on the Very Large Array (VLA) radio positions, identifying and applying shifts of $\Delta <$ 1.5 arcsec in all cases.

2.3.1 *Deblending SPIRE maps*

Owing to the coarse beam size in the SPIRE maps, to measure reliable far-IR flux densities for individual galaxies we need to deblend the SPIRE photometry for the effects of confusion. We therefore exploit the extensive multiwavelength imaging of ECDFS to construct a catalogue of IR- and radio-bright galaxies which can be used as positional priors to deblend the SPIRE maps. First, we combine the $>5\sigma$ MIPS 24 μm and radio catalogues, removing any sources within 1.5 arcsec as duplicates (in this case, we remove the lower signal-to-noise of the pair). The 1.5 arcsec offset we apply represents an acceptable trade-off between the resolution of the radio map and centring precision of the 24 μm data for a 5σ source. We then add the positions of the 99 ALMA SMGs to this catalogue, again matching any 24 μm or radio sources which lie within 1.5 arcsec (the approximate resolution of the ALMA data) of the ALESS SMG as the same ID.

To deblend the SPIRE map, we develop a Monte Carlo algorithm. At any given position in the field, we extract a thumbnail which has an extent $\pm$2.5$\times$ the FWHM of the beam at that wavelength. We then generate a new (blank) image and for each galaxy in the positional prior catalogue which lies within this area assign a random flux densities (which lies between zero and 1.3$\times$ the maximum flux density of galaxies within the thumbnail). We then convolve this image with the relevant SPIRE point spread function (PSF) and record the amplitude of the residuals and χ^2. From an initial set of 1000 models, we identify the best-fitting model (lowest χ^2). We then repeat this process, creating a new set of images with perturbed flux densities for each galaxy according to the FWHM of the flux density distribution from the previous set of models.

This process repeats until all of the models in a given iteration are within a $\Delta\chi^2 = 1\sigma$ of the best-fit. Throughout this process, we record the flux density distribution and χ^2 of every model attempted.

To ensure we do not 'overdeblend' the maps at longer wavelengths where the PSF is larger, we follow Elbaz et al. (2011) and when deblending the 350 μm image, we only include sources detected at $>2\sigma$ at 250 μm as positional priors in the 350 μm image (and similarly, for the 500 μm we only include sources $>2\sigma$ at 350 μm).

Before constructing a catalogue, we must estimate both flux density errors and upper limits for non-detections. First, we determine the detection limit by attempting to recover fake point sources which

[1] http://irsa.ipac.caltech.edu/data/SPITZER/FIDEL/

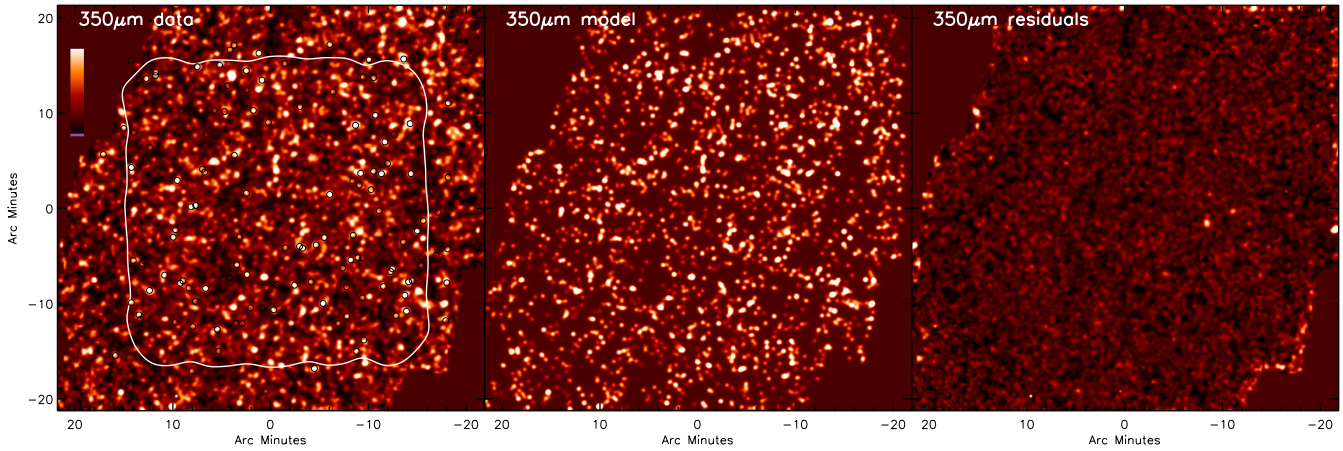

Figure 1. Left: 350 μm/SPIRE image of ECDFS. We mark the position of the LESS SMGs from Weiß et al. (2009). The contour denotes the area enclosed by the 1.2 mJy rms of the LABOCA survey (Weiß et al. 2009); Center: best-fitting 350 μm model image of the field from our deblending algorithm which uses the MIPS 24 μm, radio and ALMA positions as a positional prior catalogue; Right: 350 μm residuals between (after subtracting the best-fitting model from the data). All panels are centred at α: 03 32 32.25, δ: −27:48:17.2 (J2000) with north up and east left.

have been randomly injected into the map (and positional prior catalogue). In total, we inject ∼10 000 point sources into each of the 250, 350 and 500 μm maps (one at a time) with fluxes between 0.5 and 100 mJy and record the input ($F_{\rm in}$) and recovered ($F_{\rm out}$) flux density of the galaxy after deblending. In Fig. 1 we show the *Herschel*/SPIRE map of the ECDFS at 350μm, and in Fig. 2, we plot the fractional flux density error (($F_{\rm out} - F_{\rm in}$)/$F_{\rm in}$) as a function of $F_{\rm out}$ at each wavelength and contour the central 68 per cent of the distribution. Following Magnelli et al. (2013), we define the 3σ detection limit when 68 per cent of the distribution are recovered with a fractional error less than 30 per cent. In the ECDFS, we derive 3σ detection limits of 7.0, 8.0 and 10.6 mJy at 250, 350 and 500 μm, respectively. These are similar to the faintest fluxes reported galaxies in the ECDFS using the cross identification (XID) deblending procedure by Roseboom et al. (2010) (who derive fluxes for their faintest galaxies 6.5, 8.5 and 8.0 mJy at 250, 350 and 500 μm, respectively; Casey et al. 2012). For galaxies which are detected above 3σ, we also calculate the fractional flux density error according to the distributions shown in Fig. 2 and to be conservative, add this in quadrature to the errors derived from the family of acceptable models from the Monte Carlo deblending.

For the galaxies which have flux densities below these limits, we calculate an upper limit. This upper limit depends on its location in the map. For example, a source that lies within the beam of a nearby, brighter source is more difficult to 'detect' than an isolated source since the effective background has increased due to the emission from the nearby source and large PSF. We therefore measure the recovered flux density for all injected sources as a function of the local background in the map. Again, following Magnelli et al. (2013), we derive the upper limit by identifying where 80 per cent of the injected sources have a recovered flux density within 50 per cent of the input flux density. We show this distribution in Fig. 2 and use this distribution to assign upper limits for non-detections.

To validate the deblending (and errors), we simulate a set of SPIRE images using the SPIRE number counts and redshift distribution from Clements et al. (2010). We construct images at 250, 350 and 500 μm over a 1-square degree region (and include sources down to flux density limits of 0.5 mJy) and convolve the map with the relevant PSF. We note that we have not included any clustering of the sources in this simple analysis. To this image, we then add Gaussian noise at the same level as the SPIRE observations of the ECDFS. To construct the positional prior distribution in a comparable way to our ECDFS data, we predict the 24 μm flux density for each source injected into the fake map using its redshift and 250 μm flux density and using an far-IR SED randomly selected from the templates of Chary & Elbaz (2001). We then construct a positional prior catalogue for all sources brighter than $S_{24\,\mu\rm m} = 50$ μJy and attempt to recover the sources using our algorithm. Using this method, the ratio of the input flux density to that recovered at 250, 350 and 500 μm is $S_\lambda^{\rm in}/S_\lambda^{\rm out} = 0.96 \pm 0.02$, 0.97 ± 0.02 and 1.17 ± 0.12, respectively.

Having validated our approach, next we apply this algorithm to the ECDFS at 250, 350 and 500 μm, running the code in a grid of (overlapping) regions in ECDFS, each of extent ∼5 beams at the relevant wavelength. In Fig. 1, we show the 350 μm SPIRE map, with the positions of the LESS SMGs from Weiß et al. (2009) highlighted, as well as the best-fitting 350 μm model of the field and the residuals.[2]

From the deblended catalogue, we then extract the SPIRE photometry for the ALESS SMGs and give these in Table A1. In Fig. A1, we show example thumb-nails around four ALESS SMG in our sample, the best-fitting models and residuals at 250, 350 and 500 μm (these four galaxies are randomly selected to span the full range of 870 μm flux density from LESS; Weiß et al. 2009). In each panel, we show the positions of all of the galaxies in the 'prior' catalogue at that wavelength and also highlight the positions of the ALESS SMGs. The far-IR photometry of the ALESS SMGs (from 24 μm to 1.4 GHz) is given in Table A1. In cases where no flux is detected, we quote 3σ upper limits.

As a final check, we compare the flux densities derived for the galaxies in our prior catalogue with those recently published by Casey et al. (2012) (which are based on the 'XID' deblending procedures from Roseboom et al. 2010). Casey et al. (2012) report deblended 250, 350 and 500 μm flux densities and spectroscopic redshifts for a sample of ∼750 24 μm- and 1.4 GHz-detected

[2] The SPIRE 250, 350 and 500 μm images, best-fitting models, residual maps and deblended catalogue for all galaxies in our prior catalogue in the ECDFS (as well as the COSMOS, UDS and GOODS-North regions which we also use to validate our fluxes and errors compared to Casey et al. 2012) are available at: http://astro.dur.ac.uk/∼ams/HSOdeblend/

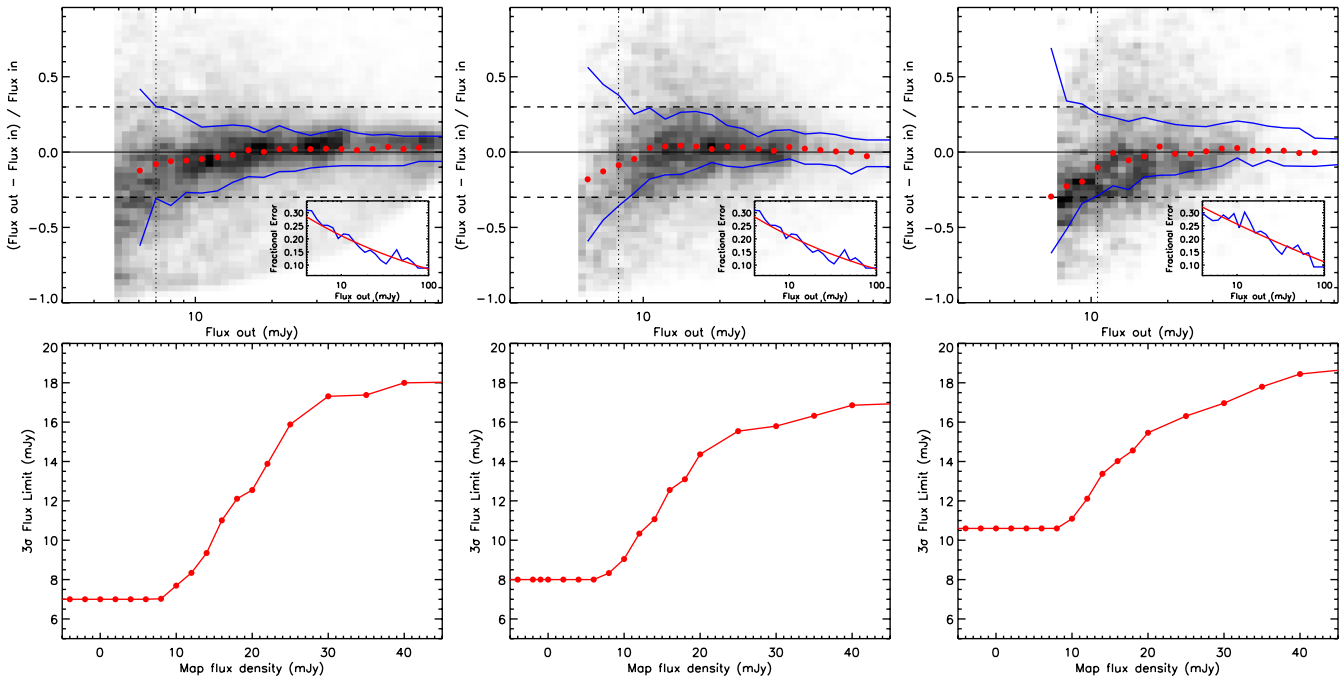

Figure 2. Top: error distributions for the deblended SPIRE maps based on the prior catalogues. These show the results from simulations for extraction of injected sources into the maps. The solid curves enclose 60 per cent of the points at each flux, and we define the detection limit as the flux density where 68 per cent of the injected galaxies are recovered with a flux density error <30 per cent (shown by the horizontal dashed lines). We derive detection limits at 250, 350 and 500 μm of 7.0, 8.0 and 10.6 mJy, respectively, as shown by the vertical dotted lines. The insets show the fractional flux density error as a function of recovered flux density (and a low-order polynomial fit) of the injected sources. These flux density fractional errors are combined with the Monte Carlo errors from the deblending to derive errors on the flux density of each galaxy. Bottom: for galaxies which are not detected in the deblended map (either because they are too faint, or they lie in the halo of a nearby 'bright' source which effectively increases the local background), we derive their 3σ upper limit by using the recovered flux density for all injected sources as a function of the local background. These limits are shown for 250, 350 and 500 μm in the lower panels.

galaxies with SPIRE counterparts in the COSMOS, ECDFS, GOODS-N and Lockman Hole regions. We cross-correlate our deblended catalogue with the Casey et al. (2012) catalogue (including our own deblended maps of the COSMOS, ECDFS and GOODS-N fields to improve the number of matches between samples) and derive comparable flux densities at all three SPIRE wavelengths, with $(F^{\lambda}_{\rm Db} - F^{\lambda}_{\rm XID})/F^{\lambda}_{\rm Db} = -0.03 \pm 0.02$, 0.08 ± 0.04 and 0.08 ± 0.10 at $\lambda = 250$, 350 and 500 μm, respectively. This suggests that the 'XID' and our deblending produce consistent flux densities to $\lesssim 10$ per cent accuracy.

3 RESULTS AND DISCUSSION

3.1 Average far-infrared colours of SMGs

Before discussing the far-IR colours of individual ALESS SMGs, we first investigate the average properties of the galaxies in our sample by stacking the multiwavelength photometry in the 'raw' (non-deblended) maps. In the PACS and SPIRE maps, we first subtract the mean flux of 1000 random positions in the map, effectively removing any systematic contribution from the background or confusion. We then stack the far-IR and radio maps at the positions of the 99 ALESS SMGs and show these results in Fig. 3 and report the average flux densities in Table 1. For the entire sample of 99 ALESS SMGs in the MAIN catalogue, the composite SED peaks at 350 μm with flux density ratios of $S_{250\ \mu{\rm m}}/S_{350\ \mu{\rm m}} = 0.8 \pm 0.1$ and $S_{350\ \mu{\rm m}}/S_{500\ \mu{\rm m}} = 1.1 \pm 0.1$, as expected for a starburst galaxy with a dust SED with characteristic dust temperature ∼30 K redshifted to $z \sim 2$.

To derive the far-IR properties of this composite dust SED, we construct a library of local galaxy templates from Chary & Elbaz (2001); Rieke et al. (2009) and Draine et al. (2007) and also add the SEDs of the well-studied high-redshift starbursts SMM J2135−0102 ($z = 2.32$) and GN 20 ($z = 4.05$) from Ivison et al. (2010) and Carilli et al. (2011), respectively, which can then be fit to the far-IR photometry. This library comprises a total of 185 templates with a range of characteristic dust temperatures (measured from the wavelength of the peak of the far-IR SED and assuming $\lambda_{\rm peak} T_{\rm d} = 2.897 \times 10^{-3}$ m.K) from $T_{\rm d} = 20$–60 K (this compilation of templates is available at the same url as the deblended catalogues).

We fit these template SEDs to the 24 μm–1.4 GHz photometry of the composite SED using a χ^2 minimization, allowing the normalization and redshift of the templates to vary. In Fig 3, we overlay the best-fit (and also show the range of models which lie within 1σ of the best fit).

A large fraction of the sub-mm sources identified in single dish observations lack radio (and/or 24 μm) counterparts, possibly as a result of the galaxies either lying at higher redshift or having colder-than-average dust temperatures. Until now, we have not known whether the unidentified SMGs have the same redshift distribution (or are representative) of the radio-identified sub-set. To provide a simple test of whether the individually radio-detected and radio-undetected sub-set show evidence for having different far-IR colours (which may indicate a redshift bias if their SEDs are similar), we stack the radio-detected (46) and radio non-detected (53) sub-sets separately and also show these in Fig. 3 (see also Table 1). Both of these sub-sets peak at 350 μm, with statistically indistinguishable

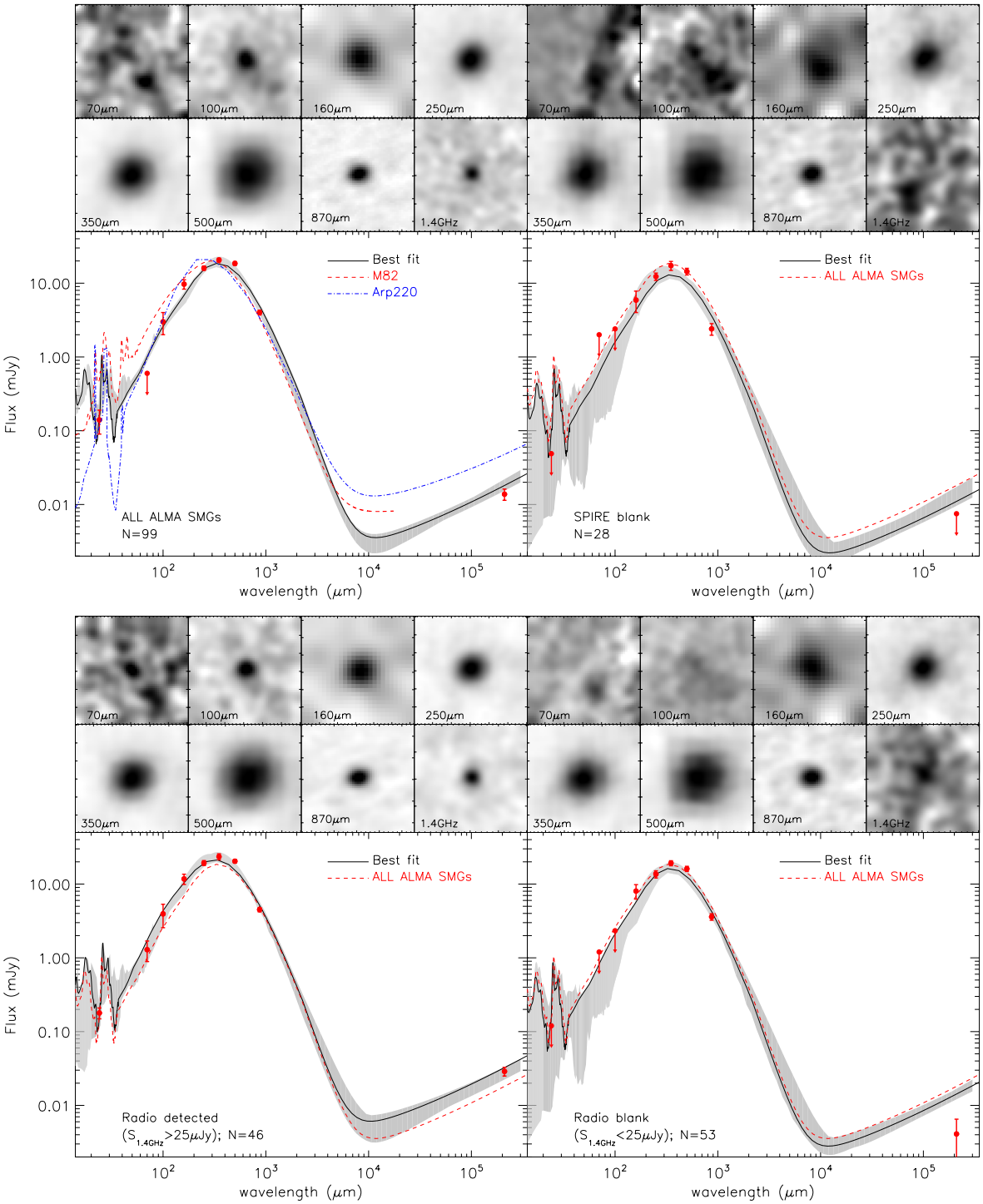

Figure 3. Top left: stacked (observed frame) spectral energy distribution for all 99 ALESS SMGs in our sample. The solid curve shows the best-fitting SED from our template library (the best-fitting template has a redshift of $z = 1.8$), with the shaded region shows the range of acceptable solutions. We also overlay the SEDs of M 82 and Arp 220 (redshifted to $z = 2.5$ and normalized to the peak). Top Right: the observed composite SED for the 34 individually SPIRE undetected ALESS SMGs. The solid curve denotes the best-fitting template (which has a best-fitting of $z = 3.5$) and the dashed curve shows the best-fitting SED to the 'All' composite in the left-hand panel. This 'SPIRE-undetected' stack appears to have the same far-IR colours as the 'All' stack, but is lower luminosity at all wavelengths. Bottom left: observed frame composite SED for the 46 individually radio-identified ALESS SMGs with the best-fitting (solid) and 'All' (dashed) composites overlaid. In this plot, the best-fitting template is for $z = 1.3$. Bottom right: the observed SED for the 53 ALESS SMGs which are (individually) non-detected at 1.4 GHz, again with the best-fitting (solid) and 'All' (dashed) composites overlaid. The best-fitting template is for $z = 3.5$. This 'radio-detected' composite SED appears to have similar 250, 350 and 500-μm colours as the 'radio non-detected' composite, although the 'radio-detected' composite has more flux at shorter (70–160 μm) wavelengths, most likely reflecting the differences in the photometric redshift distributions of the two sub-samples (assuming a fixed dust temperature). For each sample, we also show the thumb-nail images from the stacks of the *Herschel*/PACS + SPIRE (70–500 μm), ALMA 870 μm and VLA (1.4 GHz) radio. In each of these thumbnail the major tick-marks are spaced by 10 arcsec.

Table 1. Stacked far-IR photometry for ALMA SMGs.

	ALL	$S_{1.4\,\mathrm{GHz}}$ >25 μJy	$S_{1.4\,\mathrm{GHz}}$ <25 μJy
N	99	46	53
$S_{70\,\mu\mathrm{m}}$ (mJy)	<0.45 (0.1)	1.3 ± 0.4 (0.1)	<1.3 (0.1)
$S_{100\,\mu\mathrm{m}}$ (mJy)	3.0 ± 1.0 (0.1)	3.9 ± 1.4 (0.2)	<2.5 (0.2)
$S_{160\,\mu\mathrm{m}}$ (mJy)	9.7 ± 1.4 (0.3)	11.7 ± 1.9 (0.4)	8.0 ± 1.8 (0.4)
$S_{250\,\mu\mathrm{m}}$ (mJy)	16.0 ± 1.1 (0.4)	19.3 ± 1.5 (0.7)	13.6 ± 1.5 (0.5)
$S_{350\,\mu\mathrm{m}}$ (mJy)	20.6 ± 1.2 (0.5)	23.5 ± 2.2 (0.8)	19.2 ± 1.5 (0.7)
$S_{500\,\mu\mathrm{m}}$ (mJy)	18.5 ± 1.1 (0.8)	20.4 ± 1.2 (0.9)	16.1 ± 1.3 (0.8)
$S_{870\,\mu\mathrm{m}}$ (mJy)	4.0 ± 0.3 (0.4)	4.5 ± 0.31 (0.4)	3.6 ± 0.37 (0.4)
$S_{1.4\,\mathrm{GHz}}$ (μJy)	13.8 ± 2.4 (0.9)	28.9 ± 3.9 (1.3)	4.1 ± 2.4 (1.4)

Notes. The errors are those on the bootstrap of the distribution. The error in parenthesis denoted the noise in the stacked map.

350/250 μm and 350/500 μm colours. However, as can be seen from Fig. 3 and Table 1, the 70–100 μm flux densities for the radio non-detected stack are fainter than the radio-detected sub-set. For a fixed characteristic dust temperature, this may be consistent with the radio-faint sub-set of the ALESS SMGs lying at somewhat higher redshift. We will return to a discussion of this in Section 3.3.

3.2 SMGs redshifts and rest-frame composite SED

Recently, Simpson et al. (2013) used the 16-band optical–mid-IR photometric coverage of ECDFS to derive photometric redshifts for 77 of the 99 ALESS SMGs. They fitted SEDs to the 19-band (observed U to IRAC 8.0 μm) photometry using HYPER-Z with the spectral templates of Bruzual & Charlot (2003) which use using solar metallicities and employ four SFHs; a single burst (B), constant star formation (C) and two exponentially decaying SFHs with time-scales of 1 Gyr (E) and 5 Gyr (Sb). To calibrate the redshifts, Simpson et al. (2013) derive photometric redshifts of ∼6000 spectroscopically confirmed galaxies in the ECDFS, as well for spectroscopically confirmed ALESS SMGs (Danielson et al., in preparation). Simpson et al. (2013) then use the relation between rest-frame H-band magnitude and redshift for ALESS SMGs below $z = 2.5$ to crudely estimate the redshifts for a further 19 ALESS SMGs which are faint (or undetected) in the optical/near-IR, deriving a statistical redshift distribution for 96 ALESS SMGs (we note that two of the ALESS SMGs which are faint or blank in the optical/near-IR have been confirmed to be $z = 4.4$ through blind identification of [C II]; Swinbank et al. 2012). The final three ALESS SMGs from the MAIN catalogue of Hodge et al. (2013) without photometric redshifts lie outside the Multiwavelength Survey by Yale-Chile field and are only covered by IRAC, making it impossible to derive reliable photometric redshifts. Simpson et al. (2013) show that the redshift distribution of the 96 ALESS SMGs is centred at $z = 2.5 \pm 0.2$ but with a tail out to $z \gtrsim 5$, and with a typical uncertainty for any SMG of $\Delta z/(1 + z_{\mathrm{spec}}) = 0.15$. The median absolute H-band magnitude of the ALESS SMGs is $M_{\mathrm{H}} = -24.33 \pm 0.15$ which corresponds to a stellar mass of $M_{\mathrm{star}} = (8 \pm 1) \times 10^{10}\,\mathrm{M}_{\odot}$ (for an appropriate $L_{\mathrm{H}}/M_{\star}$ ratio), consistent with previous estimates of the stellar masses of SMGs (e.g. Hainline et al. 2011).

Simpson et al. (2013) used these photometric redshifts to search for differences in the redshift distribution of radio-bright versus radio-faint ALESS SMG. For the radio-detected sub-set of the population, they derive a median of $z = 2.3 \pm 0.1$ whilst for the radio-undetected sub-set, they derived $z = 3.0 \pm 0.3$. Thus, it appears that radio-faint SMGs have a redshift distribution which peaks at slightly higher redshift than the radio-detected SMGs, as expected given the positive K-correction in the radio wavebands, even though the 250/350 μm and 350/500 μm colours are indistinguishable. This is discussed in detail in Simpson et al. (2013).

We use the photometric redshifts for the 96 ALESS SMGs to derive a rest-frame UV–radio composite SED for the whole sample. For each SMG, we de-redshift the wavelength and flux density measurements (and normalize each SMG by far-IR luminosity) and then calculate a running median and show this in Fig. 4. To account for the errors on the SED at each wavelength, we bootstrap resample for both the photometric redshift and photometric errors. The best-fitting template (and 1σ error distribution) is also overlaid on to the SED in Fig. 4 which shows that the best-fitting template peaks at $\lambda_{\mathrm{rest}} = 90 \pm 5$ μm. In this plot, we also overlay the composite optical–far-IR SED derived from a sample of $z \sim 1.5$ ULIRGs with luminosities $L_{\mathrm{IR}} = 1$–$3 \times 10^{12}\,\mathrm{L}_{\odot}$ identified in the COSMOS field from Lee et al. (2013). This composite SED is reasonably well matched to the ALESS SMG composite, although shows a factor ∼1.5–2 excess in the rest-frame near- and mid-IR compared to the ALESS stack (which may be due to their sample being dominated by a 24 μm pre-selection). Nevertheless, in the rest-frame UV/optical and far-IR, both SEDs are well matched, peaking between 90–100 μm.

This well-sampled rest-frame composite SED can be used to measure the average dust masses of the ALESS SMGs. The dust mass is related to the far-IR flux density by $S_{\nu} = \kappa_{\nu}\, B_{\nu}(T)\, M_{\mathrm{d}}\, d_{\mathrm{L}}^{2}\, (1 + z)$, where S_{ν} is the flux density at frequency ν; $B_{\nu}(T)$ is the Planck function at temperature, T; κ_{ν} is the dust absorption coefficient; M_{d} is the total dust mass and d_{L} is the luminosity distance. Our sources are not perfect black bodies, but this is accounted for by the dust mass coefficient, κ_{ν} so that the grey-body is effectively represented by the product $\kappa_{\nu}\, B_{\nu}(T)$ and the luminosity of the sources at frequency ν scales as $S_{\nu}/B_{\nu}(T) \propto \nu^{2}$. The dust mass is then given by $M_{\mathrm{d}} = S_{\nu}\, \mathrm{d}_{\mathrm{L}}^{2} \,/\, (\kappa_{\nu}\, B_{\nu}(T)\, (1 + z))$.

To characterize the rest-frame composite ALESS SED in Fig. 4, we fit three dust components; cold: $T_{\mathrm{d,\,c}} = 20$–30 K; warm: $T_{\mathrm{d,\,w}} = 50$–60 K and hot $T_{\mathrm{d,\,h}} = 80$–120 K. The dust emissivity, β is allowed to vary between $\beta = 1.5$ and 2.0 (Magnelli et al. 2012a) (but is the forced to the same value for each component). From the best-fit, we derive an average cold dust mass of $M_{\mathrm{d,\,c}} = (4.1 \pm 0.6) \times 10^{8}\,\mathrm{M}_{\odot}$ (for a dust mass absorption coefficient of $\kappa_{870\,\mu\mathrm{m}} = 0.15\ \mathrm{m^{2}\ kg^{-1}}$; Weingartner & Draine 2001; Dunne, Eales & Edmunds 2003) and a ratio of $M_{\mathrm{d,\,c}}/M_{\mathrm{d,\,w}} = 30 \pm 8$ and $M_{\mathrm{d,\,w}}/M_{\mathrm{d,\,h}} > 1500$. The cold dust mass we derive from this composite is comparable to that derived for the spectroscopically confirmed SMGs, $M_{\mathrm{d}} = (3.9 \pm 0.5) \times 10^{8}\,\mathrm{M}_{\odot}$ (Magnelli et al. 2012a). However, this composite SED is derived for all ALESS SMGs (over all photometric redshifts) and so to limit any broadening of the dust SED due to selecting different SEDs at different redshifts, we also limit the composite to the redshift range $z = 1.8$–2.8. From this composite, we derive a cold dust mass of $M_{\mathrm{d,\,c}} = (4.1 \pm 0.6) \times 10^{8}\,\mathrm{M}_{\odot}$ and a ratio of $M_{\mathrm{d,\,c}}/M_{\mathrm{d,\,w}} = 43 \pm 15$ and $M_{\mathrm{d,\,w}}/M_{\mathrm{d,\,h}} > 1000$ – comparable to those derived from the composite SED of all ALESS SMGs.

3.3 Far-infrared properties of individual SMGs

Next, we investigate the properties of individual ALESS SMGs from the deblended SPIRE maps. In Fig. 4, we show example SEDs for four of the ALESS SMGs in our sample (SEDs for all ALESS SMGs can be found in Fig. A2). In cases of non-detections, we show 3σ upper limits. For each ALESS SMG, we fit the SED templates in our library to the photometry, allowing the redshift to

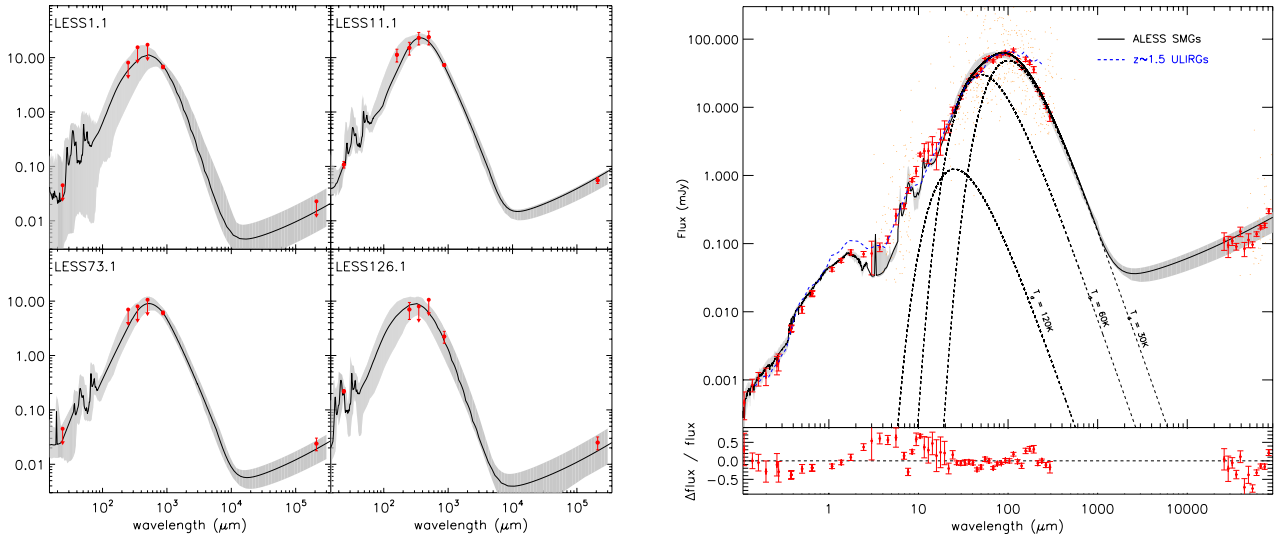

Figure 4. Left: example observed mid- to far-IR SEDs of the ALMA SMGs in our sample (one from each quartile in 870 μm LESS flux density). SEDs for all the ALESS SMGs are shown in the Appendix. In each case, the SPIRE photometry has been deblended. The solid curve shows the best-fitting SED to the 24 μm–1.4 GHz flux densities. The shaded region shows the range of acceptable solutions of these templates given the photometric redshifts (and its error). Right: rest-frame, composite SED for all ALMA SMGs in our sample from UV through to radio wavelengths. The small points show the individual measurements (and include detections and non-detections as limits). Large points denote the bootstrap median in bins of wavelength, with error bars accounting for both photometric redshift and luminosity uncertainties. The solid curve shows the best-fitting SED, with the 1σ uncertainty indicated by the shaded region, and the lower panel shows the residuals between the data and the fit. The dashed curve shows the composite SED derived from 816 $z \sim 1.5$ galaxies with luminosities $L_{\rm IR} = 1$–$3 \times 10^{12}\,{\rm L}_{\odot}$ in the COSMOS field from Lee et al. (2013). The black dashed curves show a three-component grey-body dust SED fit to the ALESS SMG composite with cold, warm and hot components with $T_{\rm d,\,c} = 20$–30 K, $T_{\rm d,\,w} = 50$–60 K and $T_{\rm d,\,h} = 80$–120 K, respectively. These grey bodies suggest an average cold dust mass of $M_{\rm d,\,c} = (4.1 \pm 0.6) \times 10^{8}\,{\rm M}_{\odot}$ (for a dust mass absorption coefficient of $\kappa_{870\,\mu{\rm m}} = 0.15\,{\rm m}^2\,{\rm kg}^{-1}$).

vary according to the photometric redshift and its error, and also accounting for the uncertainty in the photometry. Using the best-fitting dust SEDs, we calculate the IR luminosity ($L_{\rm IR}$) by integrating the rest-frame SED between 8 and 1000 μm (rest-frame). The derived far-IR luminosities (integrated between rest-frame 8 and 1000 μm) and characteristic dust temperatures ($T_{\rm d}$) of the best-fitting template from these fits are reported in Table A1 along with their photometric redshifts from Simpson et al. (2013). To facilitate a useful comparison with other surveys, we also fit the far-IR photometry of each ALESS SMG with a modified blackbody spectrum at the photometric redshift and derive the characteristic dust temperature from these fits. These dust temperatures are also reported in Table 2 and are those used in the analysis below.

Following Ivison et al. (2012), in Fig. 5 we show the far-IR (250/350 μm versus 500/350 μm and 870/500 μm) colours of the ALESS SMGs (we only plot ALESS SMGs which are detected in at least two bands). For a comparison sample, we also include the far-IR colours of SMGs with 250, 350 and 500 μm flux densities measured from Magnelli et al. (2012a). This colour–colour diagnostic is designed to crudely assess the redshift and characteristic dust temperature ($T_{\rm d}$) of galaxies detected by *Herschel*, probing their colours across the rest-frame ∼100 μm SED peak.

To assess whether these colours are consistent with those expected for dusty high-redshift galaxies, we also show as a colour scale the expected far-IR colours derived from 10^6 grey-body curves with a range of redshifts from $z = 0$ to 6, characteristic dust temperatures of $T_{\rm d} = 15$–60 K and dust emissivity $\beta = 1.0$–2.5 (we include scatter in these photometry which match the typical photometric errors in our analysis). The location of the ALESS SMGs in Fig. 5 demonstrates that their dust SEDs are consistent with a population of galaxies at $z \sim 2$–4, and we note that there are 12, 32 and 12 ALESS SMGs whose dust SEDs peak closest to 250, 350 and 500 μm, respectively (these are for those galaxies which are individually detected in at least two SPIRE bands). However, due to the dust-temperature–redshift degeneracy, there is significant scatter between the far-IR colours and photometric redshift. Indeed, as also shown in Fig. 5 the relation between 870/350 μm colour as a function of photometric redshift for the ALESS SMGs (and also including the far-IR colours of the spectroscopically confirmed SMGs from Magnelli et al. 2012a), there is approximately $\Delta z \gtrsim 1$ of scatter for a fixed 870/350-μm colour.

In Fig. 6, we show the photometric redshift distribution for ALESS SMGs, split by their far-IR colours. Crudely, for a fixed temperature, the dust SEDs for the SMGs which peak at shorter wavelengths should lie at the lower redshifts, whilst those which peak at the longer wavelengths should lie at the highest redshifts. As Fig. 6 shows, this is broadly consistent with our data; the dust SEDs of the ALESS SMGs which peak closest to 250, 350 and 500 μm peak at $z = 2.3 \pm 0.2$, 2.5 ± 0.3 and 3.5 ± 0.5, respectively. Formally, a two-sided KS test suggests a 63 per cent chance the 250 μm and 350 μm peakers are drawn from the same distribution, but only a 2.3 per cent [1.8 per cent] chance that the 350 μm and 500 μm [250 μm and 500 μm] peakers are drawn from the same population.

Finally, we note that there are 34 (out of 99) ALESS SMGs which do not have a $>3\sigma$ counterpart at 250, 350 or 500 μm. Of these 34 galaxies, 30 are also radio unidentified, and it is interesting to note that the median photometric redshift for these SPIRE and radio non-detections is higher than the full ALESS SMG sample, with $z = 3.3 \pm 0.5$ (c.f. $z = 2.5 \pm 0.2$; Simpson et al. 2013; Fig. 6). However, stacking the SPIRE maps of these 'SPIRE undetected' ALESS SMGs (Fig. 4) yields far-IR colours which peak at 350 μm with 250, 350 and 500 μm flux densities of $S_{250\,\mu{\rm m}} = 9.0 \pm 0.4$ mJy, $S_{350\,\mu{\rm m}} = 9.5 \pm 0.5$ mJy and $S_{500\,\mu{\rm m}} = 6.5 \pm 1.2$ mJy (Fig. 5). Moreover, the median 870 μm flux density of this 'SPIRE undetected' sub-set is $S_{870\,\mu{\rm m}} = 2.4 \pm 0.4$ mJy, (c.f. $S_{870\,\mu{\rm m}} = 3.4 \pm 0.3$ mJy for

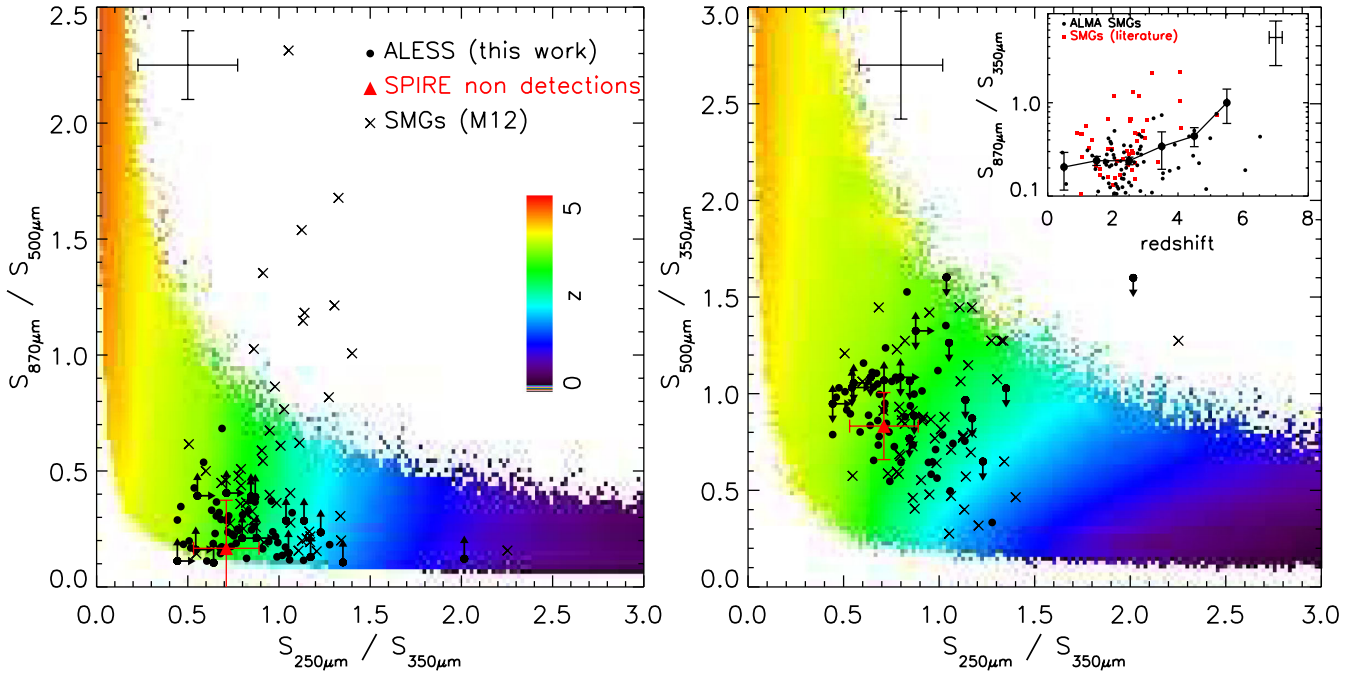

Figure 5. Far-IR colours for the ALESS SMGs. The underlying colour scale shows the expected distribution (coded by photometric redshift) for a sample of 10^7 grey-body curves with a range of temperature $T_d = 15$–60 K, dust emissivity, $\beta = 1.0$–2.5 and redshift $z = 0$–6. To account for photometry errors in the SPIRE data, these dust SEDs have 10 per cent flux density errors added to the photometry before deriving the colours. In the left-hand panel, we show the 250/350 μm versus 870/500 μm colours of ALESS SMGs and in the right-hand panel we show their 250/350 μm versus 500/350 μm colours. We only include ALESS SMGs which are detected in at least one SPIRE band (65/99 galaxies). The average colours of the remaining 34 ALESS SMGs are shown by the solid triangle using the stacking results in Fig. 3. In both panels, we show a representative error bar on the photometry in the top-left-hand corner. As evident from the figure, the ALESS SMGs have colours consistent with $z \sim 2$–4 dust SEDs. Inset: the 870/350 μm colours as a function of photometric redshift for the ALESS SMGs. In this plot, we also include the far-IR colours of the spectroscopically confirmed SMGs from Magnelli et al. (2012a, M12). In the top-right corner of this inset, we show a representative error bar on the 870/350 μm colour and redshift. The solid line shows the median (and error) in $\Delta z = 1$ bins. This shows that there is a scatter of approximately $\Delta z \gtrsim 1$ for a fixed 870/350 μm colour.

the full ALESS SMG sample). Thus, these ALESS SMGs which are undetected in the SPIRE maps appear to represent a combination of the slightly fainter and higher redshift sub-set of the ALESS SMGs, but with comparable dust temperatures. Of course, this result may partially due to our method of deblending in which we require a galaxy be detected at 250 μm to be included in the 350 μm positional prior catalogue (and a 350 μm to be included in the 500 μm positional prior catalogue) which may bias against galaxies that are faint at 250 μm and peak at longer wavelengths. However, we note that only two ALESS SMGs, ALESS 80.1 and ALESS 80.2 ($z_{phot} = 1.4$ and 2.0, respectively) have significant flux ($\gtrsim 8$ mJy at 350 μm and 500 μm) in the residual map, and therefore it does not appear that we have missed a significant fraction of ALESS SMGs in the SPIRE deblending which would bias this result.

For each ALESS SMG, we also calculate the cold dust mass using the rest-frame 870 μm luminosity from the best-fitting template and give these in Table 2. The median dust mass for all of the SMGs in our sample is $M_d = (3.6 \pm 0.3) \times 10^8\,M_\odot$, which is comparable to the average dust mass derived by Magnelli et al. (2012a) for a spectroscopic sample of SMGs, $M_d = (3.9 \pm 0.5) \times 10^8\,M_\odot$.

4 DISCUSSION

4.1 Far-infrared luminosities and star formation rates

The median IR luminosity for the ALESS SMGs is $L_{IR} = (3.0 \pm 0.3) \times 10^{12}\,L_\odot$ (corresponding to an SFR of SFR $= 310 \pm 30\,M_\odot\,yr^{-1}$ for a Chabrier IMF) with a range of $L_{IR} = 0.2$–$10 \times 10^{12}\,L_\odot$ (SFR $= 20$–$1030\,M_\odot\,yr^{-1}$). This is a factor $\sim 1.8\times$ lower than that derived for 78 spectroscopically confirmed SMGs from Chapman et al. (2005) (also derived using SPIRE photometry to constrain the dust SEDs; SFR $= 500 \pm 66\,M_\odot\,yr^{-1}$ and for the same stellar IMF; Magnelli et al. 2012a). However, this is mainly driven by the high multiplicity of SMGs due to unresolved companions in the far-IR photometry in the single dish survey. For example, Hodge et al. (2013) show that at least 35 per cent (possibly up to 50 per cent) of the LABOCA sub-mm sources are resolved by ALMA into multiple SMGs (see also Karim et al. 2013). If we instead limit the sample to ALESS SMGs whose flux is brighter than $S_{870} \geq 4.2$ mJy, then we derive an average SFR of SFR $= 530 \pm 60\,M_\odot\,yr^{-1}$.

In Fig. 7, we plot the correlation between redshift and IR luminosity for our sample. For comparison, we overlay the SMGs and 24 μm selected *Herschel* star-forming Galaxies (HSGs) from Chapman et al. (2005) and Casey et al. (2012), respectively. To highlight the selection functions on this plot, we calculate the 870 μm flux density for a dust SED with characteristic dust temperature of $T_d = 32$ K as a function of luminosity and redshift. In Fig. 7, the solid line denotes the selection limit for this dust SED with $S_{870\,\mu m} > 2$ mJy (the approximate 870 μm flux density limit of the ALESS SMG sample). However, given the apparent evolution in the luminosity–temperature plane (high-redshift ULIRGs tend to be systematically cooler than local ULIRGs at a fixed luminosity; Chapman et al. 2005; Kovács et al. 2006; Symeonidis et al. 2013), we also construct a set of dust SEDs across the redshift range $z = 0$–8 with a range of far-IR luminosities from $L_{IR} = 10^{10-14}\,L_\odot$

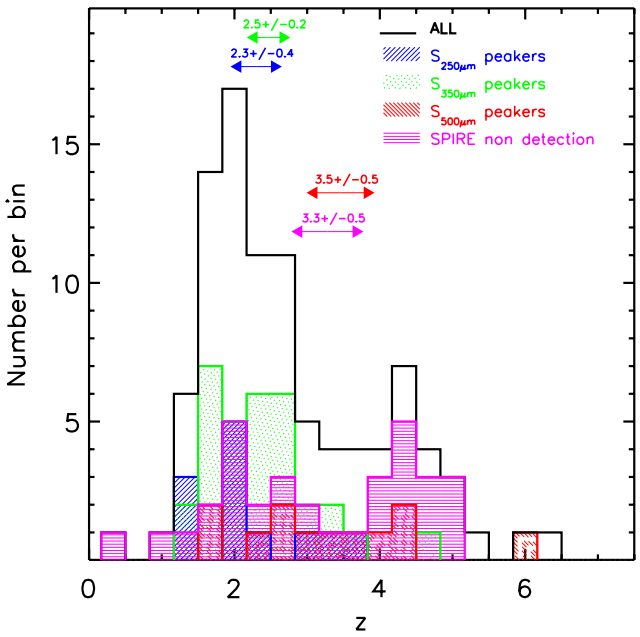

Figure 6. Photometric redshift distribution for the ALESS SMGs. The full distribution peaks at $z = 2.5 \pm 0.2$, with a tail to $z > 5$ (Simpson et al. 2013). In this plot, we also split the SMGs in to those whose observed dust SEDs peak closest to 250, 350 and 500 μm, deriving median redshifts of $z = 2.3 \pm 0.3$, 2.5 ± 0.2 and 3.5 ± 0.5, respectively (for galaxies individually detected at 350 μm). We also plot the photometric redshift distribution for the ALESS SMGs which do not have a $>3\sigma$ counterpart at 250, 350 or 500 μm, deriving a median redshift of $z = 3.3 \pm 0.5$. This plot demonstrates that those galaxies with SEDs that peak at longer far-IR wavelength, or are undetected by SPIRE, tend to lie at higher redshifts, although there is considerable overlap between the samples.

but require that the dust SEDs of higher redshift galaxies have cooler characteristic dust temperatures by $\Delta T_{\rm d}/\Delta z = 1.5$ K at a fixed luminosity. We then measure the 870 μm flux densities of each dust SED and again only record those whose 870 μm emission is above $S_{870\,\mu{\rm m}} = 2.0$ mJy. We also use the same model to estimate the selection boundary for SMGs to be detected in at least two SPIRE bands above our limits (see Section 2.3.1); we show this on Fig. 7. This final selection function highlights a steeply rising selection boundary above $z \sim 3.5$ beyond which galaxies are unlikely to be detected in at least two SPIRE bands. Nevertheless, this plot demonstrates that the ALESS SMGs apparently follow the same luminosity–redshift scaling ($L_{\rm IR} \propto (1+z)^4$) as local samples, although the luminosities appear to significantly flatten on this relation above $z \sim 2.5$.

In Fig. 7, we also show the relation between the IR luminosity and characteristic dust temperature for ALESS SMGs. In this plot, we use the characteristic dust temperature from the grey-body fits in order that a fair comparison can be made with other surveys. However, since the characteristic dust temperature is closely related to the wavelength of the peak of the dust SED, we label the axis with both dust temperature ($T_{\rm d}$) and corresponding peak wavelength ($\lambda_{\rm peak}$). In the plot, we also include measurements for SMGs from Magnelli et al. (2012a) as well as the HSGs from Casey et al. (2012) (which have a median redshift of $z \sim 0.7$), and the $z = 0$–1 SPIRE-selected LIRGs and ULIRGs from Symeonidis et al. (2013) which appear to closely follow the $z \lesssim 0.1\,L_{\rm IR}$–$T_{\rm d}$ correlated observed in the > 1.2 Jy *IRAS* 60 μm sample (Chapman et al. 2003a, see also Chapin et al. 2009). In this plot, we show a selection boundary (dashed line) that denotes the luminosity–temperature space required for an ALESS SMG with $S_{870\,\mu{\rm m}} > 2$ mJy to be detected in at least two SPIRE bands [which as recently reiterated by Symeonidis et al. (2013), drives the apparent correlation between $T_{\rm d}$ and redshift].

To test whether the ALESS SMGs have similar temperatures to local samples (at fixed luminosity), we divide the ALESS SMGs into three roughly equal number bins of $L_{\rm IR}$ and derive the average characteristic temperature of $T_{\rm d} = 25 \pm 4$, 33 ± 2 and 33 ± 1 K for $L_{\rm IR} = (1.0 \pm 0.1)$, (2.4 ± 1.3) and $(5.3 \pm 0.4) \times 10^{12}\,{\rm L}_{\odot}$, respectively. As Fig. 7 shows, for a fixed luminosity, ALESS SMGs have cooler dust temperatures ($\Delta T_{\rm d} = 3$–5 K) compared to that implied from the $L_{\rm IR}$–$T_{\rm d}$ relation from local 60 μm *IRAS* galaxies (equivalently, the dust SEDs of the ALESS SMGs peak at 10–15 μm shorter wavelengths the local *IRAS* galaxies of comparable luminosity). This offset in $T_{\rm d}$ (or $\lambda_{\rm peak}$) at fixed $L_{\rm IR}$ for high-redshift ULIRGs has also been noted by Symeonidis et al. (2013) and may be attributed to the more extended gas and dust distributions and/or higher dust masses than local galaxies of similar luminosities.

4.2 Far-infrared luminosity functions

Since our ALMA survey was carried out on a complete sample of 870 μm-selected sources lying in a single field, we can use the volume probed by our observations to derive the far-IR luminosity function of bright SMGs. To search for an evolution with redshift, we split the ALESS SMGs into three bins of photometric redshift ($z = 1.0$–2.5, $z = 2.5$–3.5 and $z = 3.5$–5.0). To account for the flux-limited nature of the LESS survey, we calculate the ALESS SMG luminosity function within an accessible volume using $\phi(L)\Delta L = \Sigma(1/V_i)$, where $\phi(L)\Delta L$ is the number density of sources with luminosities between L and $L + \Delta L$ and V_i is the comoving volume within which the ith galaxy can be detected in each luminosity bin. Errorbars are calculated by bootstrapping accounting for the uncertainties in the photometric redshifts, luminosity and binning errors. In Fig. 8, we plot the bolometric luminosity function in these three redshift bins and compare the data to a low-redshift 24 μm selected ($z < 0.3$) sample from Rodighiero et al. (2010), and the $z \sim 1.5$, 2.2 and 3.7 IR luminosity functions of 100 and 160 μm selected galaxies from the PEP survey (Gruppioni et al. 2013). As Fig. 8 shows, at fixed luminosity, SMGs have a space density at least a factor 100× that of 24-μm selected galaxies at $z < 0.3$ (Rodighiero et al. 2010).

Comparing the ALESS SMG space densities between redshifts, we also see that between $z = 1.5$–2.5 and $z = 2.5$–3.5, the ALESS SMG luminosity functions significantly overlap, although at a fixed luminosity, the higher redshift ALESS SMGs tend to have a lower space density (e.g. at a luminosity of $\sim 5 \times 10^{12}\,{\rm L}_{\odot}$, the space density of $z = 3.5$–5.0 SMGs is ∼60 per cent lower than at $z \sim 2$), implying that the volume density peaks at $z \sim 2$ and declines at higher redshift.

As noted by Weiß et al. (2009; see also Wardlow et al. 2011), the ECDFS appears to be underdense in $z \sim 2$ SMGs by a factor of ∼2× compared to other sub-millimetre surveys at flux densities $S_{870} \gtrsim 3$ mJy. To compare to other surveys, in Fig. 8 we therefore construct the luminosity function for ALESS SMGs over the redshift range $z = 1$–3.5 (to match the redshift distribution of the Chapman et al. 2005 sample) and then rescale by increasing the number density by a factor of ∼2 × to match the 850 μm number counts from those in the SHADES (Coppin et al. 2006). This rescaled $z = 1$–3.5 ALESS SMG luminosity function is well matched to the $z \sim 2.2$ luminosity functions of 100 and 160 μm selected galaxies from the PEP survey (Gruppioni et al. 2013).

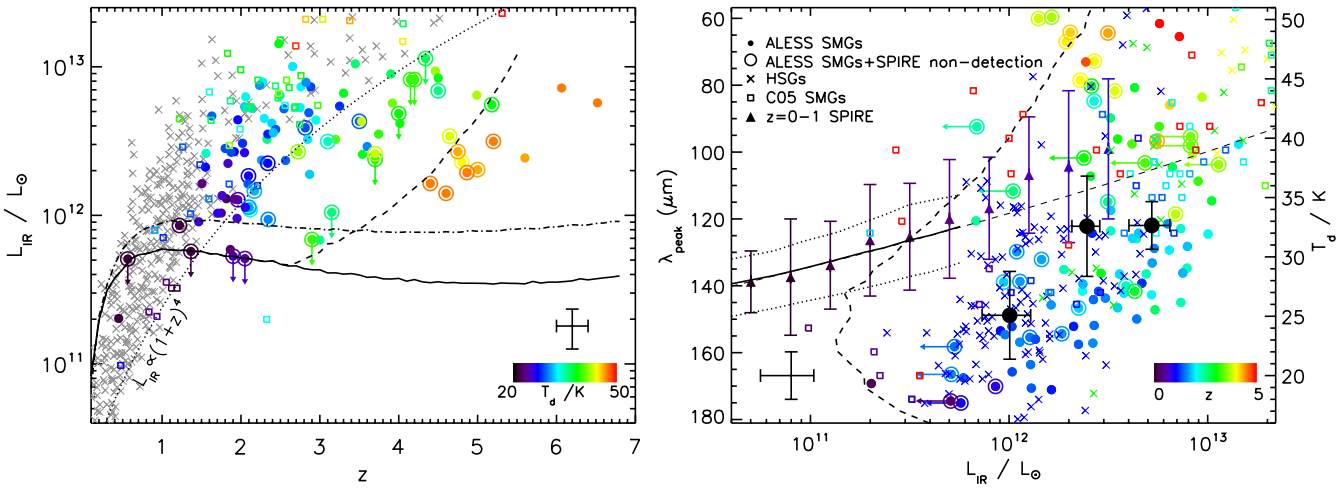

Figure 7. Left: the IR luminosity as a function of photometric redshift for the ALESS SMGs, colour coded by characteristic dust temperature. The dotted line denotes luminosity evolution according to $L_{IR} \propto (1+z)^4$. We also include several selection functions: (i) selection of an $S_{870\,\mu m} > 2$ mJy SMG for a dust SED with characteristic dust temperature of $T_d = 32$ K (solid line); (ii) selection of an $S_{870\,\mu m} > 2$ mJy SMG for a dust SED with characteristic dust temperature that evolves with luminosity and redshift (dot–dashed line) and (iii) $S_{870\,\mu m} > 2$ mJy SMGs which are likely to be detected in at least two SPIRE bands (dashed line). Right: the relation between the characteristic dust temperature (which closely corresponds to the approximate peak wavelength of the dust SED, λ_{peak}) versus IR luminosity (L_{IR}) for the ALESS SMGs, colour coded by photometric redshifts. To facilitate a useful comparison with other surveys, the characteristic dust temperatures shown here are derived using the grey-body fits to the far-IR photometry at the photometric redshift of each SMG. The dashed line denotes the approximate selection limits for an 870 μm selected sample with $S_{870\,\mu m} > 2$ mJy which are then detected in at least two SPIRE bands. We also plot the (local) 60 μm *IRAS* L_{IR}–T_d correlation from Chapman et al. (2003b) (solid line, with 1σ dispersion shown by the dotted line; see also Chapin, Hughes & Aretxaga 2009) and also the $z = 0$–1 SPIRE-selected LIRGs and ULIRGs (Symeonidis et al. 2013). In both panels, we also include recent measurements for SMGs from Magnelli et al. (2012a) which are partly based on the Chapman et al. (2005) (C05) survey and *Herschel* star-forming Galaxies (HSGs) from (Casey et al. 2012). In both panels, we also show a representative error bar for our ALESS measurements. The large, solid points in the right-hand panel show the median temperature (and bootstrap error) of ALESS SMGs in bins of far-IR luminosity, showing that the high-redshift SMGs have cooler temperatures ($\Delta T = 3$–5 K, or equivalently, their dust SEDs peak at longer wavelengths) at fixed luminosity than comparably luminous galaxies at $z = 0$, which is likely due to the more extended star formation in these systems.

4.3 The contribution of SMGs to the comoving star formation rate and stellar mass densities

We use the SFR for the galaxies in our sample to measure the contribution of SMGs to the total SFR density as a function of redshift. When calculating the SFR density, we include all of the SMGs from the ALESS MAIN catalogue with $S_{870} > 4.2$ mJy (the flux limit of the original LESS survey), and account for the factor of 2 × underdensity of SMGs in the ECDFS. As Fig. 9 shows, over the redshift range $z = 1$–5, bright ($S_{870} > 4.2$ mJy) account for ∼1–2 per cent of the total star formation density (Hopkins & Beacom 2006; Karim et al. 2011). However, we also need to account for the large fraction of the sub-millimeter galaxy population below our bright ∼4.2 mJy flux limit, by integrating down to 1 mJy. This flux represents the point at which the dust-obscured and unobscured SFR in galaxies are comparable and corresponds to an IR luminosity of $L_{IR} = 0.8 \times 10^{12}\,L_\odot$ (SFR ∼80 $M_\odot\,yr^{-1}$). We assume that the fainter SMGs ($S_{870\,\mu m} = 1$–4.2 mJy) have the same underlying redshift distribution and luminosity evolution as the bright SMGs ($S_{870\,\mu m} > 4.2$ mJy) and find that the number density of SMGs with 870 μm fluxes brighter than 1 mJy SMGs is 7× that of those brighter than 4.2 mJy (Coppin et al. 2006). Accounting for the errors in the photometric redshifts of the ALESS SMGs, and applying this correction to the number counts, in Fig. 9 we also show the contribution to the comoving SFR density from $S_{870\,\mu m} \gtrsim 1$ mJy SMGs. This shows that SMGs contribute ∼20 per cent of the total star formation over the redshift range $z = 1$–5. Of course, we note that this estimate should be considered a lower limits as we have not included ULIRGs which have comparable luminosities as the SMGs, but with hotter than average dust temperatures which makes them fainter at 870 μm, dropping them below the LESS flux limit. The contribution to the star formation density from these optical faint radio galaxies; OFRGs, (Casey et al. 2009) may increase the contribution to the SFR density for ULIRGs by a factor $\lesssim 2\times$ compared to the 870 μm-only selection we consider here.

Next, we compare these results to the semi-analytic galaxy formation model from Baugh et al. (2005) (see also Swinbank et al. 2008; González et al. 2012). This model has the advantage that it is both cosmologically based, and is required to fit the $z = 0$ *K*-band luminosity function, *IRAS* 60 μm number counts and galaxy bulge-to-disc ratios. In this model, the SMGs are dominated by bursts of star formation as a result of major mergers, with the brightest SMGs ($S_{870\,\mu m} > 5$ mJy) accounting for ∼1 per cent of the total star formation density at $z = 2$–4. Integrating all sources with $S_{870\,\mu m} > 1$ mJy this model also predicts that the fainter SMGs account for ∼20–30 per cent of the total star formation density at these redshifts (González et al. 2012). Although the use of a top heavy ($x = 0$) IMF in the model complicates this comparison, Fig. 9 shows that the GALFORM model appears to provide a reasonable description of the ALESS data over the redshift range $z \sim 1$–5.

Since the integral of the star formation history provides the total stellar mass formed in a galaxy, we also measure the fraction of stellar mass in SMGs compared to the total stellar mass density (as a function of redshift). We follow Guo et al. (2012) and obtain the global stellar mass density as a function of redshift by fitting a linear relation to the evolution of the stellar mass density from fig. 12 of Marchesini et al. (2010). Assuming the SMGs have a burst duration of 250 Myr, we calculate the duty cycle as a function of redshift

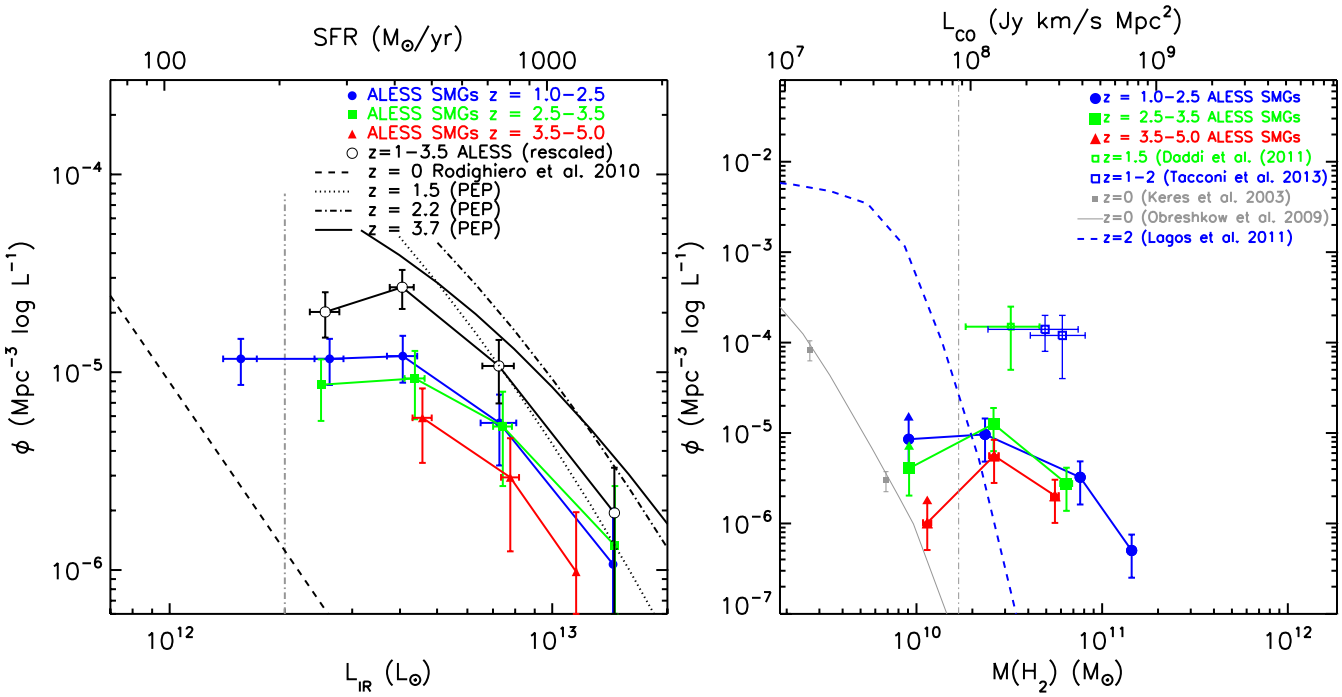

Figure 8. Left: the far-IR luminosity function for ALESS SMGs split into three bins of photometric redshift. In this plot, the error bars are derived by bootstrap resampling for uncertainties in the luminosities and photometric redshifts. Since the ECDFS has been shown to be underdense in bright sub-mm sources (Weiß et al. 2009), to match the 870 μm number counts in other extragalactic survey fields, we also re-scaled the $z = 1.5$–3.5 luminosity function by a factor 2× (black solid line). The vertical dot–dashed line shows the approximate ALESS completeness limit. We also show the $z = 0$ luminosity function from Rodighiero et al. (2010) as well as the $z \sim 1.5$, 2.2 and 3,7 IR luminosity function of 100 μm and 160 μm selected galaxies from the PEP survey from Gruppioni et al. (2013) which are well matched to the (rescaled) ALESS SMGs. Right: the H_2 mass function for SMGs compared to local data and theoretical models. In this plot, we have adopted a gas-to-dust ratio of appropriate for each galaxy given its SFR and stellar mass, and applied the correction factor for the underdensity of bright sub-mm sources in ECDFS. We compare the results for the ALESS SMGs with $z = 0$ which shows that at a fixed gas mass (or equivalently, CO(1-0) line luminosity) there are ∼100× more galaxies at $z = 2$ than $z = 0$. We also include on the plot the space density of 'main-sequence' starburst galaxies (BzKs and BX/BMs) from Daddi et al. (2010) and Tacconi et al. (2012). The dashed line shows the predicted $z = 2$ gas mass function from Lagos et al. (2011).

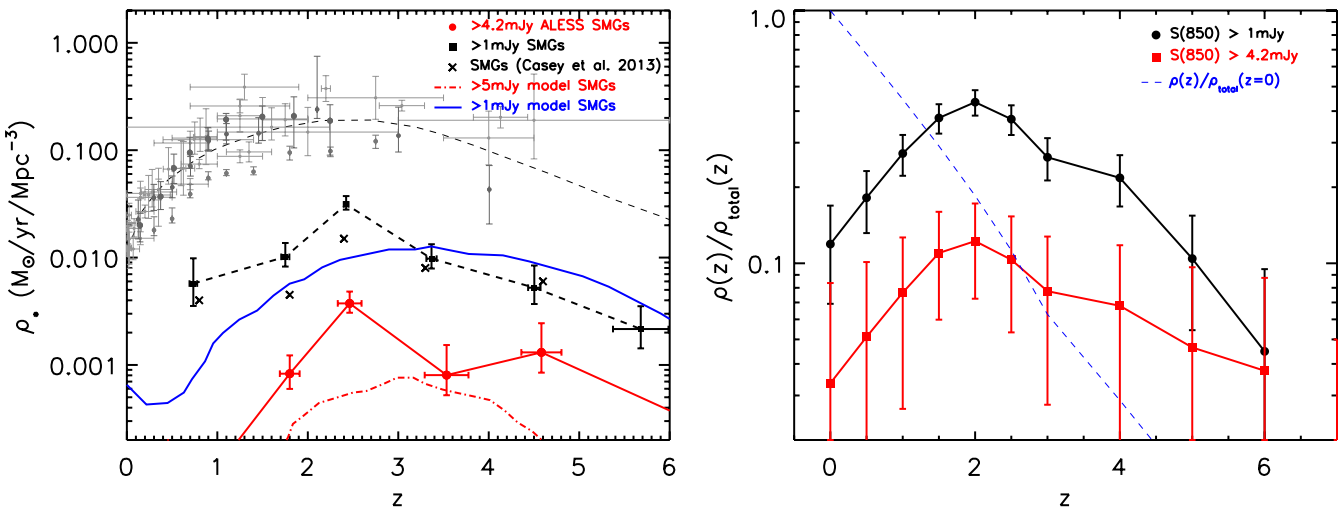

Figure 9. Left: the contribution of SMGs to the comoving cosmic star formation density as a function of redshift. Since the original LESS survey had flux density limits of $S_{870\,\mu m} = 4.2$ mJy, we only include ALESS SMGs brighter this limit, but then extrapolate to all SMGs brighter then $S_{870\,\mu m} = 1$ mJy using the 850 μm counts (Coppin et al. 2006). This plot shows that the SMG activity peaks at $z \sim 2$ – similar to that found by previous studies of star-forming galaxies and the peak activity of quasi-stellar objects (Hopkins, Richards & Hernquist 2007). The contribution from the bright SMGs to the total SFRD also peaks at $z \sim 2$ where they are responsible for ∼1–2 per cent of the Hopkins & Beacom (2006) SFRD, although extrapolating to the faintest SMGs, ∼1 mJy suggests SMGs contribute up to 20 per cent of the total SFRD at this epoch. Right: fraction of stellar mass in SMGs ($S_{870\,\mu m} > 4.2$ mJy) compared to the total stellar mass density as a function of redshift. The global stellar mass densities as a function of redshift are taken from Marchesini et al. (2010). This figure shows that at $z \gtrsim 2$–3, the bright SMGs ($S_{870\,\mu m} > 4.2$ mJy) contribute ∼15 per cent of the total stellar mass budget at that epoch, and make up 3–4 per cent of the present day stellar mass density. Integrating to fainter luminosities, SMGs with 870 μm fluxes brighter than $S_{870\,\mu m} > 1$ mJy are predicted to contribute ∼30–40 per cent of the stellar mass density at $z \sim 2$.

to infer the total stellar mass formed by SMGs (we note that the burst duration and duty cycle correction approximately trade off against each other if the burst duration does not depend on redshift) and in Fig. 9 we plot the fraction of stellar mass formed in SMGs compared to the total stellar mass density as a function of redshift for all ALESS SMGs with $S_{870} \geq 4.2$ mJy (again accounting for the factor of 2 × underdensity of the ECDFS). In this plot, we use the stellar masses for the ALESS SMGs derived by Simpson et al. (2013), which have been estimated by integrating the star formation histories and accounting for the mass-loss due to winds and supernovae. This plot shows that at $z \sim 2$–3, the bright SMGs ($S_{870} \geq 4.2$ mJy) contribute 15 per cent of the total stellar mass density at this epoch. In contrast, by $z = 0$ this plot suggests that the total stellar mass formed in bright SMGs comprises just ∼3–4 per cent of the total stellar mass density. As above, if we integrate the counts to $S_{870} \geq 1$ mJy, then as Fig. 9 shows, SMGs account for 30–40 per cent of the total stellar mass at $z \sim 2$, and ∼15 per cent of the total stellar mass density at $z = 0$.

4.4 Dust and gas mass functions

Exploiting the correlation between the dust and gas mass in local galaxies, we can also use the mass ratio of the gas-to-dust to infer the total H_2 mass in SMGs. There has been considerable interest in deriving the cold molecular gas masses in SMGs, since this provides the raw 'fuel' for star formation which determines the duration of the starburst. Most of the constraints on the gas masses have been derived from low- and mid-J ^{12}CO observations and then have to adopt CO–H_2 conversion factor (e.g. Frayer et al. 1998; Greve et al. 2005; Tacconi et al. 2006, 2008; Ivison et al. 2011; Riechers et al. 2011; Bothwell et al. 2013). In particular, Bothwell et al. (2013) used ∼3 Ms of low spatial resolution observations with Plateau de Bure Interferometer to derive the low-J ^{12}CO properties of a sample 40 luminous SMGs (detecting 32 of them). Constraining the molecular gas properties of a larger sample of SMGs, even with ALMA, will therefore require a significant investment of time. An alternative approach to estimate the gas mass is to use the (optically thin) continuum luminosity on the Rayligh–Jeans tail of the dust SED to estimate the dust mass, and then use an appropriate gas-to-dust ratio to derive the total mass of the molecular ISM. A detailed discussion of this technique and its application to both local and high-redshift galaxies is given in Scoville (2013) review.

To estimate an appropriate gas-to-dust mass ratio ($\delta_{\rm GDR}$) for SMGs, we exploit the CO-derived H_2 masses from Bothwell et al. (2013) who derive $M_{\rm H2} = 3.6 \pm 1.0 \times 10^{10}\,{\rm M}_\odot$ (including non-detections). Using far-IR and radio photometry (from 70–870 and 1.4 GHz), Magnelli et al. (2012a) fit the far-IR SEDs of many of the same galaxies to derive dust masses of $M_{\rm d} = (3.9 \pm 0.5) \times 10^8\,{\rm M}_\odot$, suggesting an average gas-to-dust ratio of $\delta_{\rm GDR} = 90 \pm 25$. For comparison, we note that the Milky Way has a gas-to-dust ratio of $\delta_{\rm GDR} \sim 130$; Jenkins 2004, whilst the gas-to-dust ratio derived for the local of star-forming galaxies (across several galaxy types) from the Spitzer Infrared Nearby Galaxy Survey from Draine et al. (2007; see also Scoville 2013) is $\delta_{\rm GDR} = 130 \pm 20$ for galaxies with metallicities above $Z/Z_\odot \gtrsim 0.2$ (which is likely to represent a lower limit for SMGs; Swinbank et al. 2004; Takata et al. 2006).

It is also possible to derive a gas-to-dust ratio for the ALESS SMGs using the stellar mass, SFR and metallicity (Z). For example, Maiolino et al. (2008) suggest a mass-metallicity–SFR plane of $Z = 8.90 + 0.47\times\, x$ with $x = \log(M_\star) - 0.32\,\log({\rm SFR}) - 10$. The gas-to-dust ratio can then be calculated by $\delta_{\rm GDR} = 10^{-0.85\,Z + 9.4}$ (Magnelli et al. 2012b). Using the SFR and stellar mass for the ALESS SMGs in our sample (Simpson et al. 2013), the average gas-to-dust ratio we derive is $\delta_{\rm GDR} = 75 \pm 10$. This is lower, but consistent within the 1σ error of that derived from the (more direct) ^{12}CO and dust masses, although we caution that the significant uncertainty in the stellar mass estimates for SMGs due to the unconstrained star formation histories may dominate the difference in $\delta_{\rm GDR}$ (Simpson et al. 2013). For simplicity, in all of the following analysis, we therefore adopt a single gas-to-dust ratio of $\delta_{\rm GDR} = 90 \pm 25$.

Applying this gas-to-dust ratio to our estimates of the dust mass, this suggests a median H_2 mass of $M_{\rm H2} = (4.2 \pm 0.4) \times 10^{10}\,{\rm M}_\odot$ for the ALESS SMGs. Together the average SFR and total H_2 mass of the SMGs suggest a gas depletion time-scale of $M_{\rm H_2}/{\rm SFR} \sim 130 \pm 15$ Myr. Assuming, on average that the burst is observed halfway through its lifetime and that the star formation remains constant over the lifetime of the burst (with no recycling of mass through supernovae or other mass-loss), this suggests a total burst duration in SMGs of ∼250 Myr (see also Greve et al. 2005; Hainline et al. 2006; Swinbank et al. 2006; Tacconi et al. 2006; Ivison et al. 2011; Riechers et al. 2011; Hickox et al. 2012; Bothwell et al. 2013), and a factor of ∼3× longer than local ULIRGs of comparable luminosity (e.g. Solomon & Sage 1988; Gao & Solomon 2004; Genzel et al. 2010).

In Fig. 8, we plot the H_2 mass function for the bright ($S_{870} \geq 4.2$ mJy) ALESS SMGs (in units of $M_{\rm H_2}/{\rm M}_\odot$ and Jy km s^{-1} Mpc^2). We also include on the plot the gas mass density of 'main-sequence' starburst galaxies (BzKs and BX/BMs) from Daddi et al. (2010) and Tacconi et al. (2010). Here, we have assumed that the six galaxies observed by Daddi et al. (2010) are representative of all star-forming BzK galaxies (although we caution that the BzKs in Daddi et al. are the most luminous sub-sample of the BzK population and so may be atypical). Nevertheless, we adopt a space density of $\phi_{\rm BzK} = (1.5 \pm 1.0) \times 10^{-4}$ Mpc^{-3} based on the average BzK space density (Daddi et al. 2005). Recently, Tacconi et al. (2012) observed a much larger sample of massive, main-sequence star-forming galaxies as part of the Plateau de Bure HIgh-z Blue Sequence Survey (PHIBSS), presenting detections of 52 star-forming galaxies between $z = 1$–1.5 and $z = 2.0$–2.5. These galaxies are selected from a parent catalogue of spectroscopically confirmed galaxies with SFR $\gtrsim 30\,{\rm M}_\odot\,{\rm yr}^{-1}$ and stellar masses of $M_\star > 2.5 \times 10^{11}\,{\rm M}_\odot$ and have gas masses of $M_{\rm H_2} = (5.5 \pm 1.8) \times 10^{10}\,{\rm M}_\odot$ (c.f. $M_{\rm H_2} = 4.2 \pm 0.4 \times 10^{10}\,{\rm M}_\odot$ for the ALESS SMGs). To estimate the space density of the parent population at these limits, we use the Bower et al. (2006) galaxy formation model (which has been shown to provide a reasonable match to the high-redshift stellar mass functions and SFR of galaxies). For the PHIBSS selection limits of SFR $\geq 30\,{\rm M}_\odot\,{\rm yr}^{-1}$, $M_\star > 2.5 \times 10^{10}\,{\rm M}_\odot$ and assuming a median reddenning of $A_{\rm V} = 0.75$ for these systems (Förster Schreiber et al. 2009), the Bower et al. (2006) model suggests space densities for the parent populations of $\phi_{z=1.0-1.5} = 1.4 \pm 0.6$ Mpc^{-3} and $\phi_{z=2.0-2.5} = 1.2 \pm 0.5$ Mpc^{-3}. Thus, the space densities of the PHIBSS galaxies and BzKs appear to be a factor of ∼8–10 × higher than the ALESS SMGs, but with comparable gas masses (Fig. 8).

In Fig. 10, we use the gas mass estimates for these samples to investigate the total H_2 contained in star-forming galaxies as a fraction of the total H_2 as a function of redshift. As above, we calculate the total gas density as a function of redshift contributed by the bright ALESS SMGs ($S_{870\,\mu{\rm m}} \geq 4.2$ mJy), and also extrapolating to fainter limits ($S_{870\,\mu{\rm m}} \geq 1$ mJy) using the sub-mm counts from Coppin et al. (2006). Of course, we caution that extrapolating to $S_{870\,\mu{\rm m}} > 1$ mJy

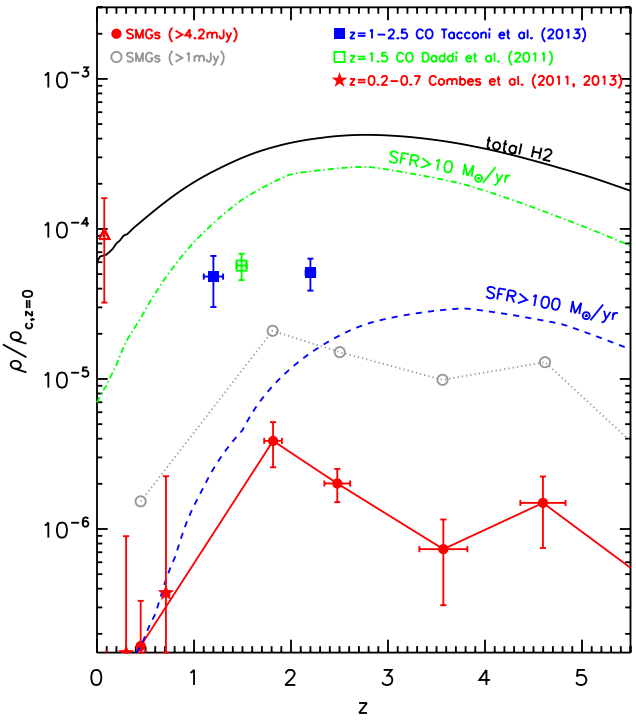

Figure 10. Global density of molecular hydrogen (normalized to the critical density at $z = 0$), as a function of redshift for ALESS SMGs and other high-redshift starburst galaxies. The solid line shows all ALESS SMGs with flux densities $S_{870\,\mu m} > 4.2$ mJy, whilst the dotted line shows the extrapolated contribution from all SMGs with flux densities $S_{870\,\mu m} > 1$ mJy. For comparison with measurements at $z = 0$, we also overlay the data from Kereš et al. (2005), as well as the model predictions for the evolution of the total gas density with redshift from Lagos et al. (2011, 2013). At $S_{870\,\mu m} > 1$ mJy (which corresponds to an SFR of approximately $\sim$100 $M_\odot$ yr^{-1} at $z \sim 2$), the SMGs contribute only $\sim$5 per cent of the total H_2. For comparisons with other high-redshift population, we also overlay the star-forming BX/BMs and BzK galaxies from Tacconi et al. (2012) and luminous BzKs from Daddi et al. (2010) which have comparable gas masses as the SMGs, but with space densities which are a factor of $\sim$10$\times$ higher. These galaxies (which have typical SFR $\gtrsim$ 80 $M_\odot$ yr^{-1}) contain 10–15 per cent of the predicted total H_2 gas budget at $z \sim$ 1–2. To provide a more detailed comparison of the contribution of galaxies with different SFR, we also overlay the model predictions from Lagos et al. (2011) and Lagos et al. (2013) for galaxies with SFR $>$ 100 $M_\odot$ yr^{-1} (which provide a reasonable match to the $>$1 mJy SMGs), and also for galaxies with SFR (SFR$>=$ 10 $M_\odot$ yr^{-1}).

assumes that the gas masses scale with the 870 μm flux, although the strong correlation between CO, dust mass and far-IR luminosity (e.g. Bothwell et al. 2013) implies that this assumption is not unreasonable.

To compare these results to other populations, we employ the $z = 0$ data from Kereš et al. (2005), who derived a total molecular gas content at $z = 0$ is $\rho/\rho_{z=0} = 0.9^{+0.8}_{-0.6}$ per cent (where $\rho_{z=0} = 3H_0^2/(8\pi G)$). For comparison samples at intermediate redshift, we exploit the observations of 36 $z \sim$ 0.2–0.6 and 39 $z \sim$ 0.6–1.0 ULIRGs from Combes et al. (2011, 2013) who derive gas masses from spectroscopy of 37 these galaxies using low-J CO emission. To estimate density of the parent population of these intermediate redshift ULIRGs (which includes optically bright and spectroscopically confirmed galaxies with $L_{IR} > 2.8 \times 10^{12}$ $L_\odot$; above the 60 μm *IRAS or* 70 μm MIPS detection limits and $\delta > -12^\circ$) using the semi-analytic GALFORM model from Baugh et al. (2005). The space density of ULIRGs with these flux limits should be $\sim$1.5 $\times$ 10^{-7} Mpc^{-3} and $\sim$7.5 $\times$ 10^{-7} Mpc^{-3} for the $z \sim$ 0.6–1.0 and $z \sim$ 0.2–0.6 populations, respectively. However, we caution that given the complex selection function and large correction factors required in this calculation, we conservatively adopt errors on the space density for this sample of at least a factor of 4$\times$ at both redshifts.

We also plot the theoretical contribution of galaxies to the total H_2 density as a function of total SFR and redshift using the semi-analytic models of Lagos et al. (2011, 2013) which is based on the semi-analytic model of Baugh et al. (2005) and Bower et al. (2006). As Fig. 10 shows, at $z \sim 2$ the bright ($\geq$4.2 mJy) ALESS SMGs contain $\sim$1 per cent of the total predicted H_2 density at $z =$ 1–3, although extrapolating to galaxies with $S_{870\,\mu m} > 1$ mJy this rises to $\sim$5 per cent. In contrast, the star-forming BzKs and BX/BM galaxies (which have typical SFR $\gtrsim$ 80 $M_\odot$ yr^{-1}) contain 10–15 per cent of the predicted total H_2 gas budget at $z \sim$ 1–2. To provide a more detailed comparison of the contribution of galaxies with different SFR, we also overlay the predictions from the model for galaxies with SFR $>$100 $M_\odot$ yr^{-1} and SFR $>=$ 10 $M_\odot$ yr^{-1}. This model provides a reasonable description of the data: model galaxies with star formation rates SFR $>$ 100 $M_\odot$ yr^{-1} (which is comparable to a $S_{870\,\mu m}$ limit of 1 mJy), should contribute $\sim$5–10 per cent of the total at $z \sim 2$, falling sharply to $<$0.1 per cent by $z = 1$.

5 CONCLUSIONS

We have exploited the multiwavelength imaging of the ECDFS to investigate the far-IR properties of a sample of 99 high-redshift, ALMA-detected sub-millimeter galaxies. These galaxies are precisely located from high-resolution ($\lesssim$1.4 arcsec) 345 GHz imaging, allowing us to measure the multiwavelength properties of the counterparts without recourse to statistical associations. Moreover, the sensitivity of the ALMA data also allow us to derive the properties of SMGs to fainter sub-mm fluxes than typically possible in single dish observations. Our main findings are as follows.

(i) Stacking the far-IR imaging at the positions of the ALESS SMGs, we show that their observed far-IR SEDs peak close to 350 μm, as expected for a high-redshift galaxy population whose dust temperatures are around $T_d \sim$ 30 K. The SPIRE colours of the individually radio-detected versus radio non-detected sub-set of the ALESS SMGs are not statistically distinguishable. However, when including the shorter wavelength PACS data, the SEDs of the radio-detected SMGs appear to peak at shorter wavelengths compared to those SMGs which are radio non-detected. For a fixed characteristic dust temperature, this is consistent with the radio-faint sub-set of the ALESS SMGs lying at higher redshift, as also confirmed by their photometric redshifts.

(ii) By deblending the SPIRE 250, 350 and 500 μm images of the ECDFS based on a 24 μm, radio and ALMA positional prior catalogue, we find that 34 (out of 99) ALESS SMGs do not have a $>3\sigma$ counterpart at 250, 350 or 500 μm. Of these 34 galaxies, 30 are also radio-undetected. These SPIRE non-detections have a median photometric redshift of $z = 3.3 \pm 0.5$ which is higher than the full ALESS SMG sample ($z = 2.5 \pm 0.2$; Simpson et al. 2013). The median photometric redshift for ALESS SMGs which are detected in at least two SPIRE bands and whose observed dust SEDs peak at 250, 350 or 500 μm are $z = 2.3 \pm 0.2$, 2.5 ± 0.3 and 3.5 ± 0.5, respectively.

(iii) We fit the far-IR SEDs of the SMGs with a suite of dust templates to derive the far-IR luminosity and hence SFR and

characteristic dust temperature. We derive a median SFR for the SMGs in our sample of SFR $= 330 \pm 30\,M_\odot\,yr^{-1}$ with a range of SFR $= 20$–$1030\,M_\odot\,yr^{-1}$. Concentrating on those ALESS SMGs whose fluxes are brighter than $S_{870} \geq 4.2$ mJy (the flux limit of the LESS survey; Weiß et al. 2009), we derive a median SFR of SFR $= 530 \pm 60\,M_\odot\,yr^{-1}$.

(iv) Accounting for the apparent underdensity of bright SMGs in ECDFS, we show that the contribution of ALESS SMGs with $S_{870\,\mu m} \geq 4.2$ mJy) to the comoving SFR density across the redshift range $z \sim 1$–4 is $\lesssim$1–2 per cent of the total. Integrating the 870 μm counts down to 1 mJy (the flux corresponding to the luminosity where the contributions from the far-IR and UV to the bolometric output of galaxies typically balance) then 870 μm-selected SMGs should account for ∼20 per cent of the total star formation across the same redshift range.

(v) By integrating the star formation histories of the SMGs in our sample (and accounting for mass-loss due to winds and supernovae), we show that bright SMGs ($S_{870} \geq 4.2$ mJy) contribute 15 per cent of the total stellar mass density at $z \sim 2$. Extrapolating to a flux limit of $S_{870} > 1$ mJy, SMGs account for 30–40 per cent of the total stellar mass density at $z \sim 2$ and ∼15 per cent of the total stellar mass at $z = 0$.

(vi) Using the rest-frame 870-μm luminosities of the ALESS SMGs, we infer an average dust masses of $M_d = (3.6 \pm 0.3) \times 10^8\,M_\odot$. Adopting a gas-to-dust ratio of $M_{H_2}/M_d = 90 \pm 25$, this suggests a typical cold gas mass of $M_{H_2} \sim (4.2 \pm 0.4) \times 10^{10}\,M_\odot$. Together the average SFR and total H_2 mass of the SMGs suggest gas depletion time-scales of M_{H_2}/SFR $= 130 \pm 15$ Myr.

(vii) Finally, we use our estimates of the H_2 mass to investigate the contribution of star-forming galaxies to the cosmic H_2 density as a function of redshift. At $z \sim 2$ the bright (> 4.2 mJy) SMGs contain 1 per cent of the total H_2, although extrapolating to $S_{870\,\mu m} > 1$mJy this rises to ∼5 per cent. We show that this is consistent with the latest theoretical models which predict that galaxies with star formation rates SFR $> 100\,M_\odot\,yr^{-1}$, should contribute ∼5–10 per cent of the total at $z \sim 2$, falling sharply to <0.1 per cent by $z = 1$.

We have presented an analysis of the far-IR and radio properties of an unbiased sample of 870 μm-selected SMGs in the ECDFS whose positions have been precisely measured with ALMA. We show that the SMGs in our sample have typical SFR of SFR $= 310 \pm 30\,M_\odot\,yr^{-1}$ and by integrating the counts to a flux limit of $S_{870} \geq 1$ mJy, we show that SMGs can account for ∼20 per cent of the comoving star formation density at $z \sim 1$–5 and estimate that these systems contain ∼10 per cent of the total molecular gas budget at this epoch. In a future paper, we will combine high-resolution *HST* and ALMA imaging of ALESS SMGs with measurements of their internal dynamics to investigate how mergers and interactions trigger the high SFR seen in these systems. Such observations will allow us to better estimate the distribution and intensity of star formation and the time-scales involved in the encounters that appear to drive the rapid star formation.

ACKNOWLEDGEMENTS

We would like to thank the referee, Catlin Casey, for a constructive report which improved the content and clarity of this paper. The ALMA observations were carried out under programme 2011.0.00294.S. ALMA is a partnership of ESO (representing its member states), NSF (USA) and NINS (Japan), together with NRC (Canada) and NSC and ASIAA (Taiwan), in cooperation with the Republic of Chile. The Joint ALMA Observatory is operated by ESO, AUI/NRAO and NAOJ. This publication is also partly based on data acquired with the APEX under programme IDs 078.F-9028(A), 079.F-9500(A), 080.A-3023(A) and 081.F-9500(A). APEX is a collaboration between the Max-Planck-Institut fur Radioastronomie, the European Southern Observatory and the Onsala Space Observatory. We also make use of data from our ESO/VLT large program (*z*LESS) PID: 183.A-0666 and VLT/XSHOOTER program 090.A.0927. This research also made use of data taken as part of the HerMES Key Programme from the SPIRE instrument team, ESAC scientists and a mission scientist. *Herschel* is an ESA space observatory with science instruments provided by European-led Principal Investigator consortia and with important participation from NASA. All of the ALMA, *Herschel*, VLA and *Spitzer* data employed in this analysis are available through the ESO, *Herschel* VLA and *Spitzer* archives. AMS gratefully acknowledges an STFC Advanced Fellowship through grant number ST/H005234/1. IRS also acknowledges STFC grant ST/I001573/1, a Leverhume Fellowship, the ERC Advanced Grant programme DUSTYGAL and a Royal Society Wolfson Merit Award. ALRD acknowledges an STFC studentship (ST/F007299/1). AK acknowledge support by the Collaborative Research Council 956, sub-project A1, funded by the Deutsche Forschungsgemeinschaft (DFG). JLW acknowledges support from Program HST-GO-12866.13-A which was provided by NASA through a grant from the Space Telescope Science Institute, which is operated by the Association of Universities for Research in Astronomy, Incorporated, under NASA contract NAS5-26555 and the Dark Cosmology Centre which is funded by the Danish National Research Foundation.

REFERENCES

Alaghband-Zadeh S. et al., 2012, MNRAS, 424, 2232
Barger A. J., Cowie L. L., Sanders D. B., Fulton E., Taniguchi Y., Sato Y., Kawara K., Okuda H., 1998, Nature, 394, 248
Barger A. J., Wang W.-H., Cowie L. L., Owen F. N., Chen C.-C., Williams J. P., 2012, ApJ, 761, 89
Baugh C. M., Lacey C. G., Frenk C. S., Granato G. L., Silva L., Bressan A., Benson A. J., Cole S., 2005, MNRAS, 356, 1191
Biggs A. D. et al., 2011, MNRAS, 413, 2314
Blain A. W., Kneib J.-P., Ivison R. J., Smail I., 1999, ApJ, 512, L87
Bothwell M. S. et al., 2013, MNRAS, 429, 3047
Bower R. G., Benson A. J., Malbon R., Helly J. C., Frenk C. S., Baugh C. M., Cole S., Lacey C. G., 2006, MNRAS, 370, 645
Bruzual G., Charlot S., 2003, MNRAS, 344, 1000
Carilli C. L., Hodge J., Walter F., Riechers D., Daddi E., Dannerbauer H., Morrison G. E., 2011, ApJ, 739, L33
Casey C. M. et al., 2009, MNRAS, 399, 121
Casey C. M. et al., 2012, ApJ, 761, 140
Casey C. M. et al., 2013, ApJ, 436, 1919
Chabrier G., 2003, PASP, 115, 763
Chapin E. L., Hughes D. H., Aretxaga I., 2009, MNRAS, 393, 653
Chapman S. C., Helou G., Lewis G. F., Dale D. A., 2003a, ApJ, 588, 186
Chapman S. C., Windhorst R., Odewahn S., Yan H., Conselice C., 2003b, ApJ, 599, 92
Chapman S. C., Blain A. W., Smail I., Ivison R. J., 2005, ApJ, 622, 772
Chary R., Elbaz D., 2001, ApJ, 556, 562
Clements D. L. A. et al., 2010, A&A, 518, L8
Combes F., García-Burillo S., Braine J., Schinnerer E., Walter F., Colina L., 2011, A&A, 528, A124
Combes F., García-Burillo S., Braine J., Schinnerer E., Walter F., Colina L., 2013, A&A, 550, A41
Coppin K. et al., 2006, MNRAS, 372, 1621

Coppin K. et al., 2008a, MNRAS, 384, 1597
Coppin K. E. K. et al., 2008b, MNRAS, 389, 45
Daddi E. et al., 2005, ApJ, 631, L13
Daddi E. et al., 2007, ApJ, 670, 156
Daddi E., Dannerbauer H., Krips M., Walter F., Dickinson M., Elbaz D., Morrison G. E., 2009, ApJ, 695, L176
Daddi E. et al., 2010, ApJ, 713, 686
Davé R., Finlator K., Oppenheimer B. D., Fardal M., Katz N., Kereš D., Weinberg D. H., 2010, MNRAS, 404, 1355
Draine B. T. et al., 2007, ApJ, 663, 866
Dunne L., Eales S. A., Edmunds M. G., 2003, MNRAS, 341, 589
Elbaz D. et al., 2011, A&A, 533, A119
Engel H. et al., 2010, ApJ, 724, 233
Förster Schreiber N. M. et al., 2009, ApJ, 706, 1364
Frayer D. T., Ivison R. J., Scoville N. Z., Yun M., Evans A. S., Smail I., Blain A. W., Kneib J.-P., 1998, ApJ, 506, L7
Gao Y., Solomon P. M., 2004, ApJS, 152, 63
Genzel R., Baker A. J., Tacconi L. J., Lutz D., Cox P., Guilloteau S., Omont A., 2003, ApJ, 584, 633
Genzel R. et al., 2010, MNRAS, 407, 2091
González J. E., Lacey C. G., Baugh C. M., Frenk C. S., Benson A. J., 2012, MNRAS, 423, 3709
Granato G. L., Silva L., Lapi A., Shankar F., De Zotti G., Danese L., 2006, MNRAS, 368, L72
Greve T. R. et al., 2005, MNRAS, 359, 1165
Gruppioni C. et al., 2013, MNRAS, 432, 23
Guo Y., Giavalisco M., Cassata P., Ferguson H. C., Williams C. C., Dickinson M., Koekemoer A., Grogin N. A., 2012, ApJ, 749, 149
Hainline L. J., Blain A. W., Greve T. R., Chapman S. C., Smail I., Ivison R. J., 2006, ApJ, 650, 614
Hainline L. J., Blain A. W., Smail I., Alexander D. M., Armus L., Chapman S. C., Ivison R. J., 2011, ApJ, 740, 96
Hayward C. C., Kereš D., Jonsson P., Narayanan D., Cox T. J., Hernquist L., 2011, ApJ, 743, 159
Hayward C. C., Jonsson P., Kereš D., Magnelli B., Hernquist L., Cox T. J., 2012, MNRAS, 424, 951
Hickox R. C. et al., 2012, MNRAS, 421, 284
Hodge J. A. et al., 2013, ApJ, 768, 91
Hopkins A. M., Beacom J. F., 2006, ApJ, 651, 142
Hopkins P. F., Richards G. T., Hernquist L., 2007, ApJ, 654, 731
Hughes D. H. et al., 1998, Nature, 394, 241
Huynh M. T. et al., 2013, MNRAS, 431, L88
Ivison R. J. et al., 2002, MNRAS, 337, 1
Ivison R. J. et al., 2005, MNRAS, 364, 1025
Ivison R. J. et al., 2007, MNRAS, 380, 199
Ivison R. J. et al., 2010, A&A, 518, L35
Ivison R. J., Papadopoulos P. P., Smail I., Greve T. R., Thomson A. P., Xilouris E. M., Chapman S. C., 2011, MNRAS, 412, 1913
Ivison R. J. et al., 2012, MNRAS, 425, 1320
Jenkins E. B., 2004, in McWilliam A., Rauch M., eds, Origin and Evolution of the Elements. Cambridge Univ. Press, Cambridge, p. 336
Karim A. et al., 2011, ApJ, 730, 61
Karim A. et al., 2013, MNRAS, 432, 2
Kereš D., Katz N., Weinberg D. H., Davé R., 2005, MNRAS, 363, 2
Kovács A., Chapman S. C., Dowell C. D., Blain A. W., Ivison R. J., Smail I., Phillips T. G., 2006, ApJ, 650, 592
Lagos C. D. P., Lacey C. G., Baugh C. M., Bower R. G., Benson A. J., 2011, MNRAS, 416, 1566
Lagos C. d. P., Baugh C. M., Zwaan M. A., Lacey C. G., Gonzalez-Perez V., Power C., Swinbank A. M., van Kampen E., 2013, MNRAS, preprint (arXiv:1310.4178)
Lee N. et al., 2013, ApJ, 778, 131
Lilly S. J., Eales S. A., Gear W. K. P., Hammer F., Le Fèvre O., Crampton D., Bond J. R., Dunne L., 1999, ApJ, 518, 641
Lindner R. R. et al., 2011, ApJ, 737, 83
Lutz D. et al., 2011, A&A, 532, A90
Magnelli B. et al., 2012a, A&A, 539, A155
Magnelli B. et al., 2012b, A&A, 548, A22
Magnelli B. et al., 2013, A&A, 553, A132
Maiolino R. et al., 2008, A&A, 488, 463
Marchesini D. et al., 2010, ApJ, 725, 1277
McMullin J. P., Waters B., Schiebel D., Young W., Golap K., 2007, in Shaw R. A., Hill F., Bell D. J., eds, ASP Conf. Ser., Vol. 376, Astronomical Data Analysis Software and Systems XVI. Astron. Soc. Pac., San Francisco, p. 127
Miller N. A. et al., 2013, ApJS, 205, 13
Narayanan D., Cox T. J., Hayward C. C., Younger J. D., Hernquist L., 2009, MNRAS, 400, 1919
Noeske K. G. et al., 2007, ApJ, 660, L43
Oliver S. J. et al., 2012, MNRAS, 424, 1614
Pope A. et al., 2006, MNRAS, 370, 1185
Riechers D. A., Hodge J., Walter F., Carilli C. L., Bertoldi F., 2011, ApJ, 739, L31
Rieke G. H., Alonso-Herrero A., Weiner B. J., Pérez-González P. G., Blaylock M., Donley J. L., Marcillac D., 2009, ApJ, 692, 556
Rodighiero G. et al., 2010, A&A, 518, L25
Rodighiero G. et al., 2011, ApJ, 739, L40
Roseboom I. G. et al., 2010, MNRAS, 409, 48
Sanders D. B., Mirabel I. F., 1996, ARA&A, 34, 749
Scoville N., 2013, in Wong T., Ott J., eds, Proc. IAU Symp. 292, Molecular Gas, Dust, and Star Formation. Cambridge Univ. Press, Cambridge, p. 279
Simpson J. et al., 2013, ApJ, preprint (arXiv:1310.6363)
Smail I., Ivison R. J., Blain A. W., 1997, ApJ, 490, L5
Smolčić V. et al., 2012, ApJS, 200, 10
Solomon P. M., Sage L. J., 1988, ApJ, 334, 613
Spergel D. N. et al., 2007, ApJS, 170, 377
Swinbank A. M., Smail I., Chapman S. C., Blain A. W., Ivison R. J., Keel W. C., 2004, ApJ, 617, 64
Swinbank A. M., Chapman S. C., Smail I., Lindner C., Borys C., Blain A. W., Ivison R. J., Lewis G. F., 2006, MNRAS, 371, 465
Swinbank A. M. et al., 2008, MNRAS, 391, 420
Swinbank A. M. et al., 2010, MNRAS, 405, 234
Swinbank A. M. et al., 2012, MNRAS, 427, 1066
Symeonidis M. et al., 2013, MNRAS, 431, 2317
Tacconi L. J. et al., 2006, ApJ, 640, 228
Tacconi L. J. et al., 2008, ApJ, 680, 246
Tacconi L. J. et al., 2010, Nature, 463, 781
Tacconi L. J. et al., 2012, ApJ, 768, 74
Takata T., Sekiguchi K., Smail I., Chapman S. C., Geach J. E., Swinbank A. M., Blain A., Ivison R. J., 2006, ApJ, 651, 713
Wang W.-H., Cowie L. L., Barger A. J., Williams J. P., 2011, ApJ, 726, L18
Wang S. X. et al., 2013, ApJ, 778, 179
Wardlow J. L. et al., 2011, MNRAS, 415, 1479
Weingartner J. C., Draine B. T., 2001, ApJ, 548, 296
Weiß A. et al., 2009, ApJ, 707, 1201

APPENDIX A: EXAMPLE SPIRE IMAGES, MODELS AND RESIDUALS FOR LESS REGIONS

In Fig. A1, we show the SPIRE 250, 350 and 500 μm images, models and residual maps for four LESS SMG regions whose far-IR SEDs are shown in Fig. 4.

In Table A1, we provide the ID, far-IR and radio fluxes for the 96 ALESS SMGs which have photometric redshifts in our sample. We also list their derived properties, dust mass, far-IR luminosity and characteristic dust temperature.

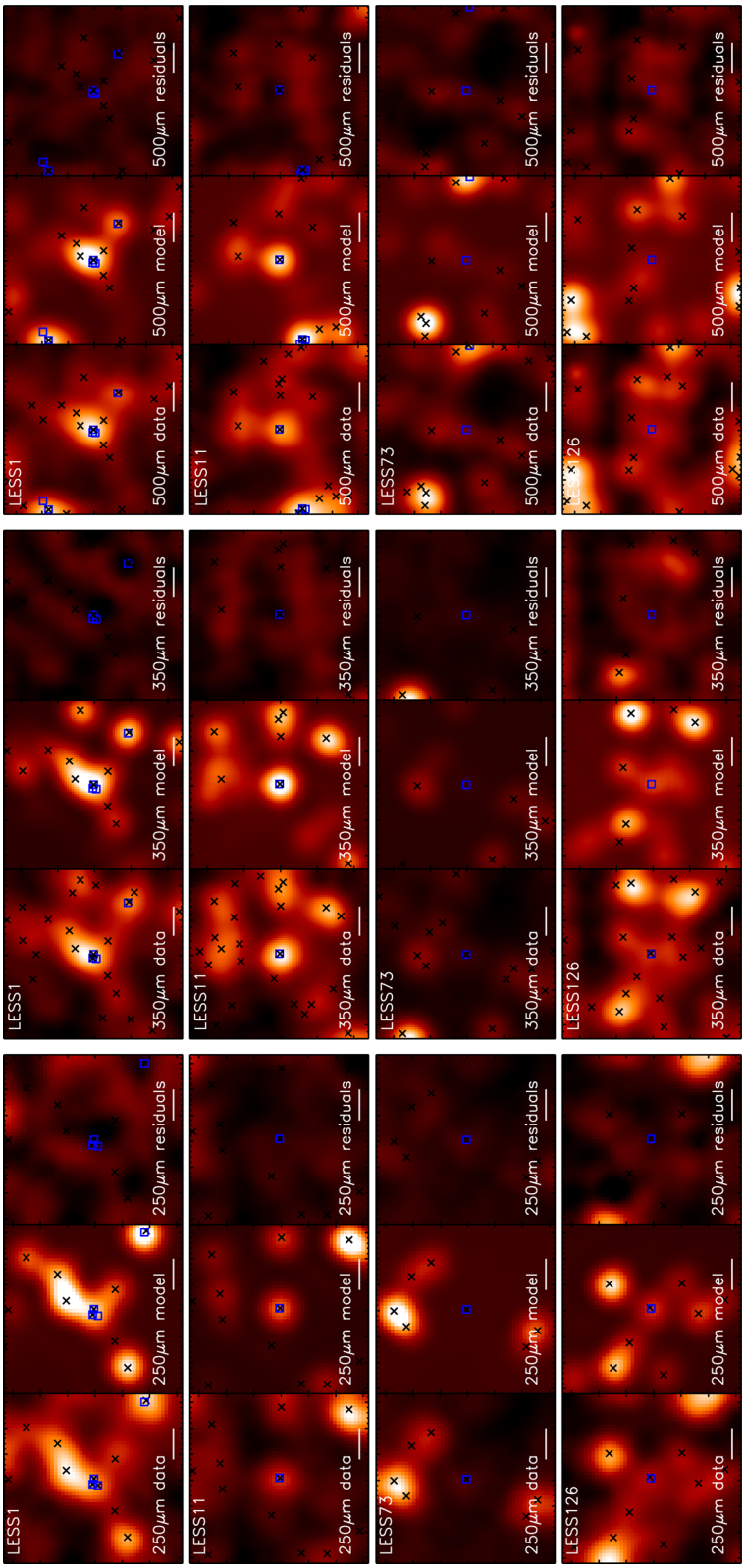

Figure A1. Example 250, 350 and 500 μm images, models and residuals for the ALMA SMGs in our sample. These postage stamps show the images for the four ALMA SMGs whose SEDs are shown in Fig. 4. For each image, the data, model and residuals are on the same colour scale. In the 'data' panel, black crosses denote the galaxies in the positional prior catalogue for that wavelength (only galaxies detected at $>2\sigma$ at 250 μm are used in deblending the 350 μm and similarly for 500 μm). To highlight this, in the 'model' and 'residuals' panels, black crosses denote those galaxies which are detected at that wavelength above the flux limits (see Section 3). In all panels, we mark the positions of the ALESS SMGs as squares. The 250, 350 and 500 μm images are 1.7, 2.5 and 3.4 arc-minutes across, respectively (∼6 beams in each case).

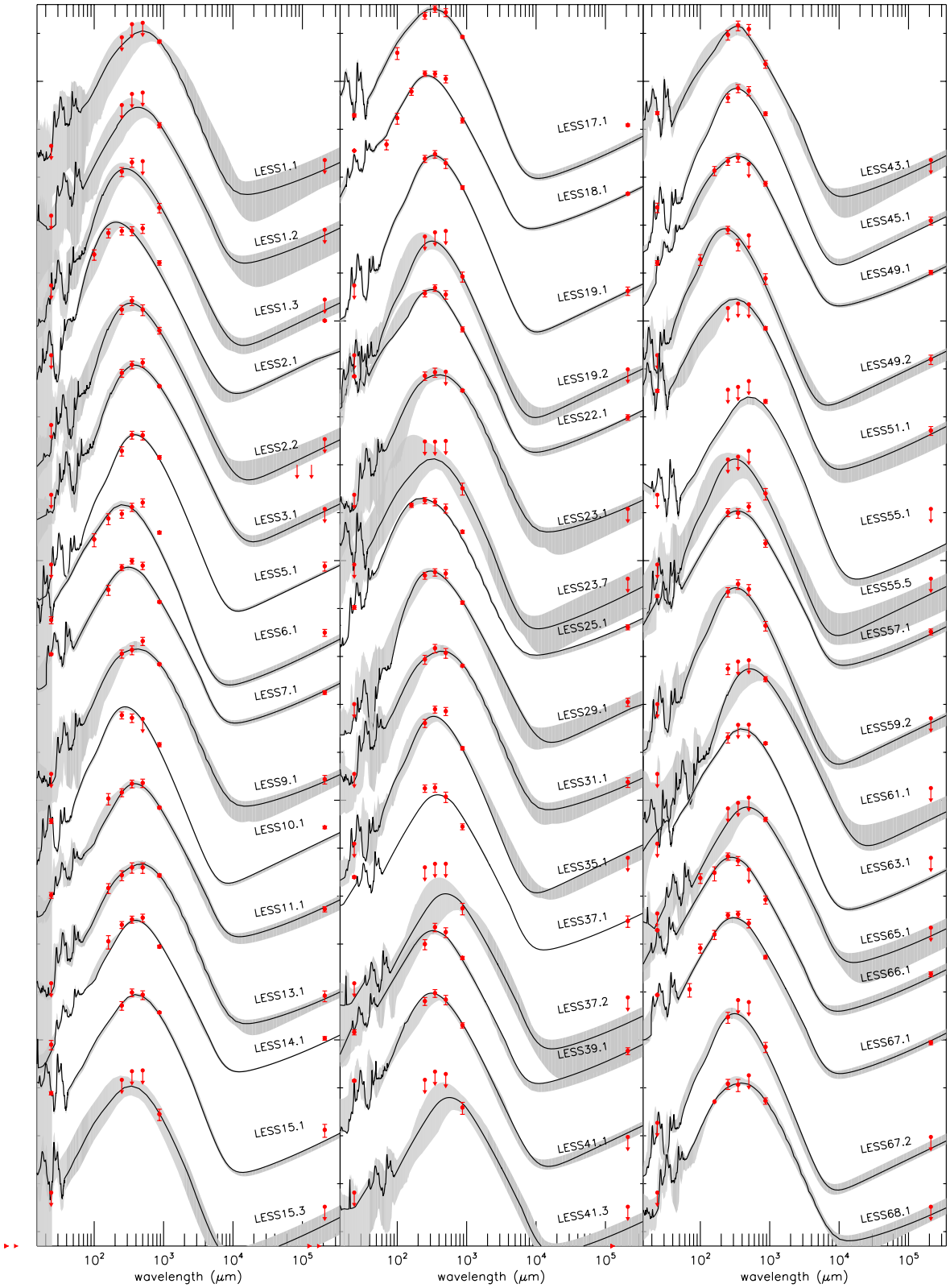

Figure A2. SEDs of the ALMA SMGs in our sample. In each case, the SPIRE photometry has been deblended. The solid black curve shows the best-fitting SED, and the grey region shows the range of acceptable solutions.

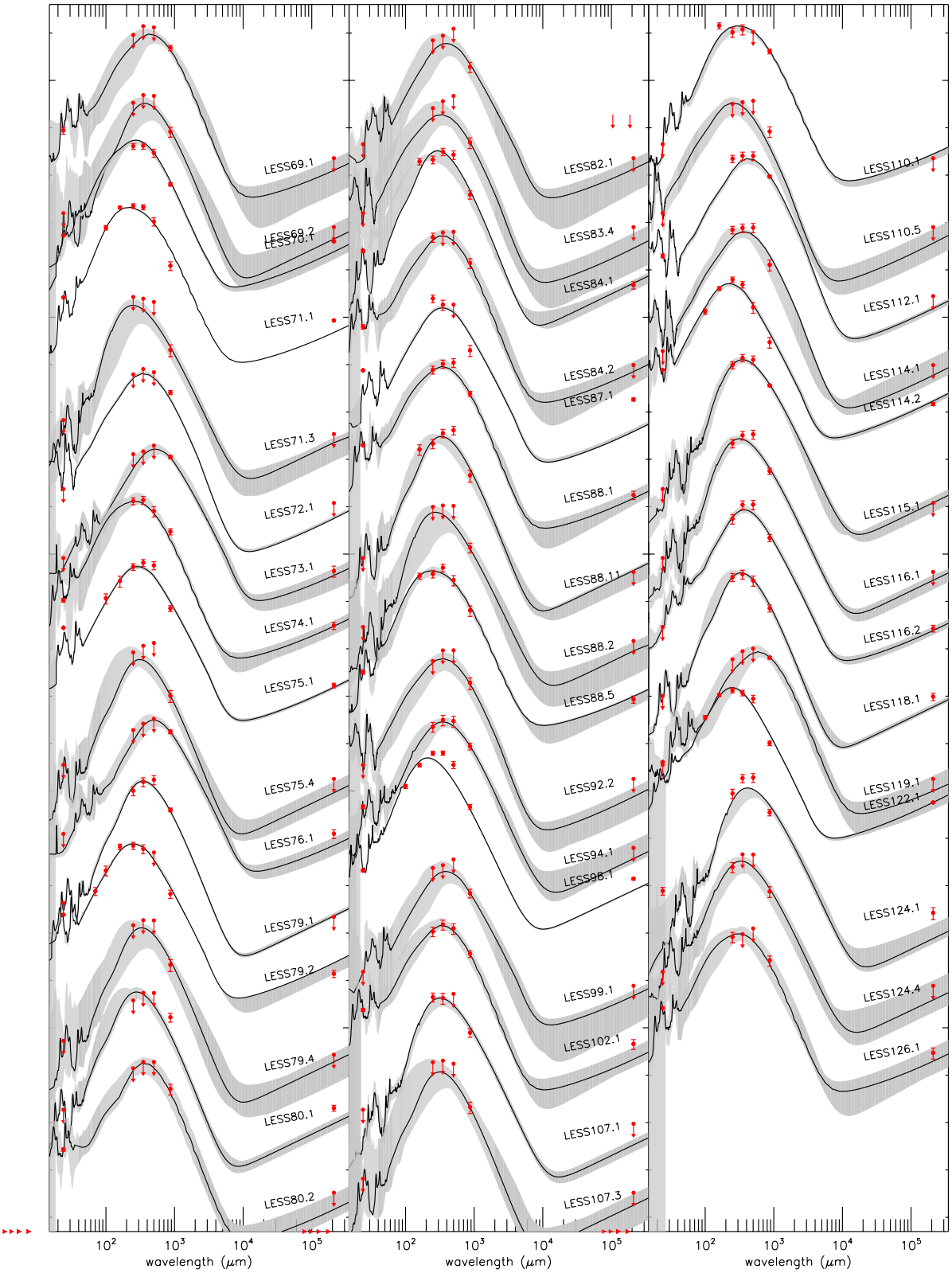

Figure A2 – *continued*

Table A1. Far-infrared and radio flux densities of ALESS SMGs and their derived properties.

ID	$S_{870\,\mu m}$ (mJy)	$S_{1.4\,GHz}$ (μJy)	$S_{500\,\mu m}$ (mJy)	$S_{350\,\mu m}$ (mJy)	$S_{250\,\mu m}$ (mJy)	$S_{24\,\mu m}$ (mJy)	z_{phot}	$\log(M_{dust})$	$L_{8-1000\,\mu m}$ ($\times 10^{12}\,L_\odot$)	T_d[a] (K)
LESS1.1	6.75 ± 0.49	<22.8	<16.65	<15.59	<8.30	<45.0	$4.34^{+2.66}_{-1.43}$	9.13 ± 0.03	$3.3^{+7.7}_{-1.6}$	36[24]
LESS1.2	3.48 ± 0.43	< 22.8	< 16.65	< 15.59	< 9.14	< 45.0	$4.65^{+2.34}_{-1.02}$	8.86 ± 0.05	$3.4^{+2.9}_{-1.6}$	44[32]
LESS1.3	1.89 ± 0.42	< 22.8	< 17.62	16.69 ± 3.57	10.70 ± 2.31	< 45.0	$2.85^{+0.20}_{-0.30}$	8.25 ± 0.09	$3.2^{+1.2}_{-1.8}$	31[40]
LESS2.1	3.81 ± 0.42	236.90 ± 7.90	19.90 ± 4.29	17.78 ± 3.76	17.66 ± 3.21	< 45.0	$1.96^{+0.27}_{-0.20}$	8.39 ± 0.05	$4.4^{+0.0}_{-1.2}$	24[40]
LESS2.2	4.23 ± 0.67	< 22.8	11.53 ± 2.93	17.62 ± 3.71	11.58 ± 2.46	< 45.0	$3.92^{+0.48}_{-1.42}$	8.68 ± 0.06	$5.6^{+2.1}_{-3.2}$	42[37]
LESS3.1	8.28 ± 0.40	< 22.8	25.80 ± 5.03	23.33 ± 4.29	15.68 ± 2.93	< 45.0	$3.90^{+0.50}_{-0.59}$	8.98 ± 0.02	$9.0^{+4.7}_{-3.0}$	36[35]
LESS5.1	7.78 ± 0.68	41.70 ± 8.80	22.47 ± 4.61	22.90 ± 4.25	10.57 ± 2.33	< 45.0	$2.86^{+0.05}_{-0.04}$	8.54 ± 0.04	$4.9^{+0.4}_{-0.7}$	27[38]
LESS6.1	5.98 ± 0.41	48.90 ± 8.10	25.29 ± 4.95	20.45 ± 3.99	14.72 ± 2.83	89.65 ± 15.00	$0.45^{+0.06}_{-0.04}$	8.25 ± 0.03	$0.2^{+0.1}_{-0.0}$	11[19]
LESS7.1	6.10 ± 0.32	78.60 ± 7.10	34.95 ± 6.12	43.60 ± 5.74	32.16 ± 4.54	494.70 ± 15.00	$2.50^{+0.12}_{-0.16}$	8.99 ± 0.02	$6.4^{+1.2}_{-0.9}$	31[32]
LESS9.1	8.75 ± 0.47	34.80 ± 7.10	26.60 ± 5.15	17.43 ± 3.66	14.50 ± 2.78	< 45.0	$4.50^{+0.54}_{-2.33}$	9.08 ± 0.02	$8.4^{+7.1}_{-3.5}$	38[32]
LESS10.1	5.25 ± 0.50	98.70 ± 6.30	< 18.04	19.01 ± 3.87	21.61 ± 3.58	133.75 ± 15.00	$2.02^{+0.09}_{-0.09}$	8.42 ± 0.04	$3.1^{+0.1}_{-0.3}$	26[38]
LESS11.1	7.29 ± 0.41	55.40 ± 6.90	23.82 ± 4.75	23.04 ± 4.23	15.12 ± 2.85	108.16 ± 15.00	$2.83^{+1.88}_{-0.50}$	8.84 ± 0.02	$7.9^{+0.7}_{-1.9}$	29[33]
LESS13.1	8.01 ± 0.59	24.80 ± 6.30	11.73 ± 2.90	11.77 ± 2.89	8.09 ± 1.90	< 45.0	$3.25^{+0.64}_{-0.46}$	8.92 ± 0.03	$5.4^{+2.3}_{-1.7}$	26[24]
LESS14.1	7.47 ± 0.52	91.20 ± 8.10	29.99 ± 5.53	27.63 ± 4.64	21.35 ± 3.52	67.35 ± 15.00	$4.47^{+2.54}_{-0.88}$	9.15 ± 0.03	$9.4^{+0.6}_{-0.3}$	42[33]
LESS15.1	9.01 ± 0.37	32.10 ± 9.70	21.11 ± 4.39	23.57 ± 4.29	12.62 ± 2.58	186.09 ± 15.00	$1.93^{+0.62}_{-0.33}$	9.51 ± 0.02	$1.3^{+2.7}_{-0.2}$	21[19]
LESS15.3	1.95 ± 0.52	< 22.8	< 15.93	< 15.33	< 10.14	< 45.0	$3.15^{+0.65}_{-0.65}$	8.65 ± 0.10	$1.5^{+2.8}_{-0.5}$	35[19]
LESS17.1	8.44 ± 0.46	122.20 ± 7.00	27.57 ± 5.24	32.58 ± 5.04	23.60 ± 3.78	194.86 ± 15.00	$1.51^{+0.10}_{-0.07}$	9.38 ± 0.02	$1.6^{+0.5}_{-0.1}$	20[19]
LESS18.1	4.38 ± 0.54	129.40 ± 6.90	32.24 ± 5.81	40.96 ± 5.60	41.70 ± 5.30	1020.42 ± 15.00	$2.04^{+0.10}_{-0.06}$	8.79 ± 0.05	$5.4^{+0.8}_{-0.8}$	30[33]
LESS19.1	4.98 ± 0.42	34.70 ± 6.90	16.02 ± 3.63	24.85 ± 4.41	19.90 ± 3.38	< 45.0	$2.41^{+0.17}_{-0.11}$	8.41 ± 0.04	$3.6^{+0.4}_{-0.5}$	30[38]
LESS19.2	1.98 ± 0.47	< 22.8	< 17.62	< 16.50	< 13.50	< 45.0	$2.17^{+0.09}_{-0.10}$	8.01 ± 0.09	$1.5^{+1.3}_{-0.5}$	30[38]
LESS22.1	4.48 ± 0.54	65.20 ± 8.60	23.75 ± 4.74	32.70 ± 5.05	25.03 ± 3.88	465.14 ± 15.00	$1.88^{+0.18}_{-0.23}$	9.08 ± 0.05	$2.7^{+2.5}_{-0.4}$	27[24]
LESS23.1	6.74 ± 0.37	< 22.8	< 16.65	16.20 ± 3.51	13.71 ± 2.72	< 45.0	$4.99^{+2.01}_{-2.55}$	9.01 ± 0.02	$6.4^{+4.9}_{-2.7}$	43[35]
LESS23.7	1.76 ± 0.49	< 22.8	< 17.07	< 16.49	< 16.64	< 45.0	$2.90^{+1.20}_{-0.40}$	8.69 ± 0.11	$3.0^{+1.6}_{-2.0}$	40[19]
LESS25.1	6.21 ± 0.47	63.40 ± 7.60	19.40 ± 4.13	26.13 ± 4.52	28.01 ± 4.19	164.17 ± 15.00	$2.24^{+0.07}_{-0.17}$	8.43 ± 0.03	$7.5^{+0.4}_{-1.2}$	29[41]
LESS29.1	5.90 ± 0.43	49.80 ± 9.60	23.96 ± 4.77	25.57 ± 4.47	21.71 ± 3.56	< 45.0	$2.66^{+2.94}_{-0.76}$	8.47 ± 0.03	$10.0^{+0.9}_{-5.4}$	31[41]
LESS31.1	8.12 ± 0.37	30.40 ± 6.90	15.12 ± 3.46	18.85 ± 3.79	11.06 ± 2.34	< 45.0	$2.89^{+1.80}_{-0.41}$	8.68 ± 0.02	$7.3^{+5.3}_{-2.9}$	26[32]
LESS37.1	2.92 ± 0.41	31.50 ± 8.40	12.28 ± 3.00	18.99 ± 3.81	18.34 ± 3.22	258.49 ± 15.00	$3.53^{+0.56}_{-0.31}$	8.87 ± 0.06	$4.3^{+0.3}_{-0.5}$	44[32]
LESS37.2	1.65 ± 0.44	< 22.8	< 14.00	< 13.97	< 11.80	< 45.0	$4.87^{+0.21}_{-0.40}$	8.52 ± 0.10	$1.9^{+2.1}_{-1.2}$	55[32]
LESS39.1	4.33 ± 0.34	49.80 ± 8.10	15.01 ± 3.45	19.04 ± 3.81	8.44 ± 2.01	122.49 ± 15.00	$2.44^{+0.17}_{-0.23}$	8.70 ± 0.03	$3.8^{+0.4}_{-0.8}$	27[32]
LESS41.1	4.88 ± 0.61	< 22.8	16.76 ± 3.73	22.84 ± 4.21	15.57 ± 2.92	340.47 ± 15.00	$2.75^{+4.25}_{-0.72}$	8.68 ± 0.05	$5.3^{+0.4}_{-2.7}$	31[35]
LESS41.3	2.68 ± 0.75	< 22.8	< 13.42	< 15.04	< 10.14	< 45.0	$3.10^{+1.30}_{-0.60}$	8.36 ± 0.11	$1.9^{+3.4}_{-0.8}$	33[32]
LESS43.1	2.30 ± 0.42	< 22.8	12.30 ± 3.04	14.71 ± 3.34	9.40 ± 2.17	218.09 ± 15.00	$1.71^{+0.20}_{-0.12}$	8.79 ± 0.07	$1.0^{+0.7}_{-0.2}$	23[23]
LESS45.1	6.03 ± 0.54	35.50 ± 6.70	18.22 ± 3.95	20.51 ± 3.96	12.94 ± 2.57	66.93 ± 15.00	$2.34^{+0.26}_{-0.67}$	8.38 ± 0.04	$3.5^{+0.2}_{-0.5}$	26[38]
LESS49.1	6.00 ± 0.68	84.50 ± 8.40	< 15.41	20.88 ± 4.08	17.65 ± 3.25	133.14 ± 15.00	$2.76^{+0.11}_{-0.14}$	8.73 ± 0.05	$7.3^{+0.8}_{-2.3}$	32[32]
LESS49.2	1.80 ± 0.46	37.00 ± 8.20	< 14.29	9.28 ± 2.53	18.70 ± 3.29	< 45.0	$1.47^{+0.07}_{-0.10}$	7.94 ± 0.10	$0.9^{+0.7}_{-0.2}$	23[38]
LESS51.1	4.70 ± 0.39	34.50 ± 7.20	< 14.86	< 15.33	< 12.37	231.94 ± 15.00	$1.22^{+0.03}_{-0.06}$	8.96 ± 0.03	$0.9^{+0.3}_{-0.3}$	17[19]
LESS55.1	3.99 ± 0.36	< 22.8	< 10.60	< 8.00	< 7.00	< 45.0	$2.05^{+0.15}_{-0.13}$	8.90 ± 0.04	$0.5^{+0.0}_{-0.1}$	21[19]
LESS55.2	2.35 ± 0.60	< 22.8	< 10.60	< 8.00	< 7.00	< 45.0	$4.20^{+0.50}_{-0.90}$	8.96 ± 0.10	$2.4^{+1.6}_{-1.3}$	40[19]
LESS55.5	1.37 ± 0.37	< 22.8	< 10.60	< 8.00	< 7.00	< 45.0	$2.35^{+0.11}_{-0.13}$	7.89 ± 0.10	$0.9^{+1.2}_{-0.4}$	28[38]
LESS57.1	3.56 ± 0.61	51.00 ± 7.20	20.71 ± 4.32	15.31 ± 3.41	15.85 ± 2.97	283.72 ± 15.00	$2.95^{+0.05}_{-0.10}$	8.86 ± 0.07	$4.4^{+0.8}_{-0.7}$	32[32]
LESS59.2	1.94 ± 0.44	< 22.8	11.24 ± 2.83	14.42 ± 3.28	9.89 ± 2.21	< 45.0	$2.09^{+0.78}_{-0.29}$	8.02 ± 0.09	$1.6^{+1.8}_{-0.3}$	27[38]
LESS61.1	4.29 ± 0.51	< 22.8	< 10.60	< 9.94	7.06 ± 1.76	< 45.0	$6.52^{+0.36}_{-0.34}$	8.65 ± 0.05	$5.7^{+2.6}_{-2.2}$	52[37]
LESS63.1	5.59 ± 0.35	< 22.8	< 13.71	< 13.56	7.44 ± 1.79	< 45.0	$1.87^{+0.10}_{-0.33}$	9.19 ± 0.03	$0.6^{+0.1}_{-0.0}$	20[19]
LESS65.1	4.16 ± 0.43	< 22.8	< 11.79	< 9.15	< 7.00	< 45.0	$2.82^{+0.95}_{-0.36}$	8.47 ± 0.04	$3.9^{+1.8}_{-1.7}$	27[32]
LESS66.1	2.50 ± 0.48	69.80 ± 8.10	< 10.60	16.33 ± 3.49	20.07 ± 3.42	576.23 ± 15.00	$2.33^{+0.05}_{-0.04}$	8.67 ± 0.08	$3.2^{+0.4}_{-0.6}$	35[33]
LESS67.1	4.50 ± 0.38	73.90 ± 6.90	22.99 ± 4.63	35.68 ± 5.26	33.68 ± 4.61	732.63 ± 15.00	$2.14^{+0.05}_{-0.09}$	8.85 ± 0.04	$5.3^{+0.7}_{-1.3}$	31[32]
LESS67.2	1.73 ± 0.41	< 22.8	< 14.86	< 16.37	7.22 ± 1.87	< 45.0	$2.05^{+0.06}_{-0.16}$	7.88 ± 0.09	$1.1^{+0.3}_{-0.5}$	24[38]
LESS68.1	3.70 ± 0.56	< 22.8	< 12.58	8.07 ± 2.31	8.38 ± 1.98	< 45.0	$3.60^{+1.10}_{-1.10}$	8.58 ± 0.06	$3.4^{+1.7}_{-1.1}$	28[32]
LESS69.1	4.85 ± 0.63	< 22.8	< 13.14	< 13.97	< 9.14	87.91 ± 15.00	$2.34^{+0.27}_{-0.44}$	8.63 ± 0.05	$2.2^{+0.3}_{-1.5}$	25[24]
LESS69.2	2.36 ± 0.56	< 22.8	< 13.42	< 13.97	< 9.62	< 45.0	$4.75^{+0.35}_{-1.05}$	8.71 ± 0.09	$2.6^{+2.5}_{-1.0}$	48[35]

Table A1 – *continued*

ID	$S_{870\,\mu m}$ (mJy)	$S_{1.4\,GHz}$ (μJy)	$S_{500\,\mu m}$ (mJy)	$S_{350\,\mu m}$ (mJy)	$S_{250\,\mu m}$ (mJy)	$S_{24\,\mu m}$ (mJy)	z_{phot}	log (M_{dust})	$L_{8-1000\,\mu m}$ ($\times 10^{12}$ L$_\odot$)	T_d[a] (K)
LESS69.3	2.05 ± 0.56	< 22.8	< 13.14	< 12.68	< 7.00	< 45.0	$4.80^{+0.30}_{-1.10}$	9.02 ± 0.10	$2.3^{+2.1}_{-0.9}$	45[19]
LESS70.1	5.23 ± 0.45	325.40 ± 7.60	24.09 ± 4.78	33.89 ± 5.13	33.25 ± 4.61	436.16 ± 15.00	$2.28^{+0.05}_{-0.06}$	8.78 ± 0.04	$7.9^{+0.8}_{-1.2}$	31[33]
LESS71.1	2.85 ± 0.60	199.00 ± 8.70	24.41 ± 4.83	49.13 ± 6.02	51.97 ± 5.98	609.47 ± 15.00	$2.48^{+0.21}_{-0.11}$	8.62 ± 0.08	$14.3^{+0.0}_{-0.9}$	38[52]
LESS71.3	1.36 ± 0.38	< 22.8	< 14.00	< 16.42	< 17.82	< 45.0	$2.73^{+0.22}_{-0.25}$	8.22 ± 0.11	$2.7^{+1.0}_{-1.7}$	42[41]
LESS72.1	4.91 ± 0.50	< 22.8	< 13.14	< 15.33	< 11.80	< 45.0	$4.15^{+0.55}_{-1.65}$	9.13 ± 0.04	$4.1^{+4.1}_{-2.6}$	40[19]
LESS73.1	6.09 ± 0.47	24.00 ± 6.30	< 10.60	< 8.00	< 7.00	< 45.0	$5.18^{+0.43}_{-0.45}$	8.97 ± 0.03	$5.6^{+1.8}_{-1.1}$	38[32]
LESS74.1	4.64 ± 0.69	48.00 ± 8.20	12.52 ± 3.06	21.47 ± 4.12	20.57 ± 3.45	164.91 ± 15.00	$1.80^{+0.13}_{-0.13}$	8.27 ± 0.06	$2.8^{+0.0}_{-1.0}$	27[38]
LESS75.1	3.17 ± 0.45	74.90 ± 8.50	25.68 ± 5.01	29.18 ± 4.80	23.99 ± 3.84	1240.04 ± 15.00	$2.39^{+0.08}_{-0.06}$	8.86 ± 0.06	$4.2^{+0.9}_{-0.4}$	31[32]
LESS75.4	1.30 ± 0.37	< 22.8	< 16.87	< 14.71	< 10.68	< 45.0	$2.10^{+0.29}_{-0.34}$	7.89 ± 0.11	$1.1^{+1.5}_{-0.6}$	29[38]
LESS76.1	6.42 ± 0.58	45.40 ± 9.50	< 12.04	< 9.53	< 7.00	< 45.0	$4.50^{+0.20}_{-2.00}$	8.83 ± 0.04	$6.8^{+1.1}_{-1.9}$	35[33]
LESS79.1	4.12 ± 0.37	< 22.8	17.89 ± 3.92	16.11 ± 3.52	10.47 ± 2.29	< 45.0	$2.04^{+0.63}_{-0.31}$	8.13 ± 0.04	$2.6^{+0.2}_{-0.4}$	24[38]
LESS79.2	1.98 ± 0.40	40.90 ± 7.00	< 14.86	17.72 ± 3.74	20.78 ± 3.52	719.92 ± 15.00	$1.55^{+0.11}_{-0.18}$	8.41 ± 0.08	$2.1^{+0.6}_{-0.0}$	25[32]
LESS79.4	1.81 ± 0.51	< 22.8	< 15.68	< 15.81	< 12.37	< 45.0	$4.60^{+1.20}_{-0.60}$	8.46 ± 0.11	$1.9^{+2.6}_{-0.7}$	51[38]
LESS80.1	4.03 ± 0.86	48.80 ± 7.00	< 13.14	< 13.13	< 9.14	< 45.0	$1.96^{+0.16}_{-0.14}$	8.01 ± 0.08	$1.3^{+0.4}_{-0.3}$	22[38]
LESS80.2	3.54 ± 0.90	< 22.8	< 13.14	< 13.13	< 9.62	185.31 ± 15.00	$1.37^{+0.17}_{-0.08}$	8.72 ± 0.10	$0.4^{+0.5}_{-0.2}$	18[19]
LESS82.1	1.93 ± 0.47	< 22.8	< 12.31	< 8.80	< 7.00	< 45.0	$2.10^{+3.27}_{-0.44}$	8.15 ± 0.09	$1.8^{+1.4}_{-1.0}$	24[32]
LESS83.4	1.39 ± 0.36	< 22.8	< 13.42	< 10.37	< 7.41	< 45.0	$0.57^{+1.54}_{-0.50}$	7.81 ± 0.10	$0.3^{+0.6}_{-0.3}$	13[19]
LESS84.1	3.17 ± 0.63	38.90 ± 6.80	21.99 ± 4.50	25.53 ± 4.47	17.34 ± 3.22	204.78 ± 15.00	$1.92^{+0.09}_{-0.07}$	8.27 ± 0.08	$2.7^{+0.3}_{-0.7}$	24[38]
LESS84.2	3.25 ± 0.77	< 22.8	< 14.86	< 14.36	11.36 ± 2.49	146.23 ± 15.00	$1.75^{+0.08}_{-0.19}$	8.60 ± 0.09	$1.0^{+0.4}_{-0.5}$	20[24]
LESS87.1	1.34 ± 0.35	122.30 ± 9.30	< 12.31	12.28 ± 2.96	16.58 ± 3.04	504.78 ± 15.00	$3.20^{+0.08}_{-0.47}$	8.78 ± 0.10	$3.2^{+0.2}_{-0.5}$	41[32]
LESS87.3	2.44 ± 0.59	< 22.8	< 10.60	< 9.15	< 7.00	< 45.0	$4.00^{+1.10}_{-0.30}$	8.93 ± 0.09	$2.5^{+1.9}_{-1.0}$	39[19]
LESS88.1	4.62 ± 0.58	33.60 ± 6.80	20.96 ± 4.38	19.71 ± 3.94	14.82 ± 2.83	378.07 ± 15.00	$1.84^{+0.12}_{-0.11}$	8.67 ± 0.05	$2.2^{+0.8}_{-0.8}$	22[24]
LESS88.11	2.51 ± 0.71	< 22.8	22.44 ± 4.57	19.37 ± 3.92	11.71 ± 2.62	< 45.0	$2.57^{+0.04}_{-0.12}$	8.29 ± 0.11	$2.3^{+2.2}_{-0.6}$	27[38]
LESS88.2	2.14 ± 0.50	< 22.8	< 16.18	< 16.47	< 15.50	< 45.0	$5.20^{+0.60}_{-1.20}$	8.62 ± 0.09	$2.3^{+3.1}_{-1.0}$	60[37]
LESS88.5	2.86 ± 0.72	38.20 ± 6.60	12.56 ± 3.08	22.98 ± 4.26	17.05 ± 3.13	143.40 ± 15.00	$2.30^{+0.11}_{-0.50}$	8.29 ± 0.10	$4.5^{+1.2}_{-0.9}$	31[41]
LESS92.2	2.42 ± 0.68	< 22.8	< 11.79	< 11.76	< 7.00	< 45.0	$1.90^{+0.28}_{-0.75}$	9.01 ± 0.11	$0.4^{+0.2}_{-0.2}$	22[19]
LESS94.1	3.18 ± 0.52	< 22.8	10.87 ± 2.76	11.44 ± 2.85	8.19 ± 1.92	168.21 ± 15.00	$2.87^{+0.37}_{-0.64}$	8.94 ± 0.07	$1.9^{+2.0}_{-0.6}$	30[24]
LESS98.1	4.78 ± 0.60	145.00 ± 8.20	36.86 ± 6.33	65.47 ± 6.65	64.74 ± 6.76	217.63 ± 15.00	$1.63^{+0.17}_{-0.09}$	8.67 ± 0.05	$4.7^{+0.7}_{-0.0}$	27[35]
LESS99.1	2.05 ± 0.43	< 22.8	< 10.60	< 8.00	< 7.00	< 45.0	$5.00^{+1.20}_{-0.60}$	8.59 ± 0.08	$2.2^{+2.1}_{-0.8}$	48[32]
LESS102.1	3.08 ± 0.50	38.50 ± 9.10	10.65 ± 2.70	12.79 ± 3.03	9.16 ± 2.08	202.01 ± 15.00	$1.76^{+0.16}_{-0.18}$	8.56 ± 0.06	$1.4^{+0.8}_{-0.6}$	22[24]
LESS103.3	1.43 ± 0.41	< 22.8	< 14.86	< 12.68	< 10.14	< 45.0	$4.40^{+0.70}_{-0.70}$	8.82 ± 0.11	$1.6^{+1.8}_{-0.7}$	49[19]
LESS107.1	1.91 ± 0.39	< 22.8	< 12.58	10.24 ± 2.67	10.77 ± 2.32	< 45.0	$3.75^{+0.09}_{-0.08}$	8.28 ± 0.08	$3.5^{+1.1}_{-0.8}$	40[41]
LESS107.3	1.46 ± 0.40	< 22.8	< 12.04	< 13.97	< 12.94	< 45.0	$2.12^{+1.54}_{-0.81}$	7.88 ± 0.10	$1.1^{+2.5}_{-0.9}$	31[38]
LESS110.1	4.11 ± 0.47	< 22.8	< 10.60	11.96 ± 2.89	10.41 ± 2.33	< 45.0	$2.55^{+0.70}_{-0.50}$	8.28 ± 0.05	$5.2^{+0.7}_{-1.0}$	27[40]
LESS110.5	2.39 ± 0.60	< 22.8	< 10.60	< 9.94	< 9.14	< 45.0	$3.70^{+0.40}_{-1.20}$	8.94 ± 0.10	$2.3^{+2.0}_{-1.3}$	39[19]
LESS112.1	7.62 ± 0.49	< 22.8	20.82 ± 4.33	20.86 ± 4.02	18.13 ± 3.20	161.26 ± 15.00	$1.95^{+0.15}_{-0.26}$	9.36 ± 0.03	$1.0^{+0.2}_{-0.0}$	23[19]
LESS114.1	2.99 ± 0.78	< 22.8	18.20 ± 4.00	17.95 ± 3.71	16.34 ± 2.97	< 45.0	$3.00^{+1.40}_{-0.50}$	8.86 ± 0.10	$6.2^{+1.3}_{-3.9}$	34[19]
LESS114.2	1.98 ± 0.50	97.80 ± 6.80	10.87 ± 2.80	32.58 ± 5.07	41.62 ± 5.37	513.43 ± 15.00	$1.56^{+0.07}_{-0.07}$	8.64 ± 0.10	$2.6^{+1.0}_{-0.3}$	33[32]
LESS116.1	3.08 ± 0.47	< 22.8	18.41 ± 3.98	17.53 ± 3.65	11.89 ± 2.43	< 45.0	$3.54^{+1.47}_{-0.87}$	8.51 ± 0.06	$2.6^{+3.5}_{-0.2}$	38[38]
LESS116.2	3.42 ± 0.57	41.90 ± 6.80	17.26 ± 3.83	17.09 ± 3.60	8.67 ± 2.00	< 45.0	$4.02^{+1.19}_{-2.19}$	8.80 ± 0.07	$4.2^{+1.0}_{-0.7}$	39[33]
LESS118.1	3.20 ± 0.54	43.50 ± 7.80	12.30 ± 3.00	16.71 ± 3.56	14.43 ± 2.79	< 45.0	$2.26^{+0.50}_{-0.23}$	8.24 ± 0.07	$2.4^{+0.7}_{-0.3}$	29[38]
LESS119.1	8.27 ± 0.54	< 22.8	< 12.85	< 11.29	< 7.65	< 45.0	$3.50^{+0.95}_{-0.35}$	8.95 ± 0.03	$4.3^{+3.7}_{-2.6}$	27[24]
LESS122.1	3.69 ± 0.42	207.50 ± 7.40	32.08 ± 5.79	42.54 ± 5.70	48.26 ± 5.73	1479.99 ± 15.00	$2.06^{+0.05}_{-0.06}$	8.90 ± 0.05	$6.3^{+0.4}_{-0.5}$	32[33]
LESS124.1	3.64 ± 0.57	27.70 ± 7.80	19.83 ± 4.19	19.25 ± 3.84	9.16 ± 2.09	80.41 ± 15.00	$6.07^{+0.94}_{-1.16}$	8.69 ± 0.06	$7.2^{+1.1}_{-2.5}$	54[41]
LESS124.4	2.24 ± 0.58	< 22.8	< 13.42	< 13.56	7.31 ± 1.78	< 45.0	$5.60^{+0.60}_{-1.20}$	8.56 ± 0.10	$4.3^{+1.3}_{-1.3}$	48[35]
LESS126.1	2.23 ± 0.55	25.10 ± 6.70	< 10.60	< 8.00	7.02 ± 1.75	219.61 ± 15.00	$1.82^{+0.28}_{-0.08}$	8.29 ± 0.10	$1.3^{+0.5}_{-0.7}$	19[24]

Notes. 3σ upper limits are given in the case of non-detections. [a] We provide two estimates of the dust temperature; the first value corresponds to the characteristic dust temperature as measured from a modified blackbody fit to the far-infrared photometry at the photometric redshift. The second value (in parenthesis) corresponds to the wavelength of the peak of the best-fitting dust SED template and assuming $\lambda_{peak} T_d = 2.897 \times 10^{-3}$ m.K.

This paper has been typeset from a TEX/LATEX file prepared by the author.